
A MULTILEVEL STOCHASTIC-GRADIENT NEURAL SOLVER FOR BOUNDARY INTEGRAL EQUATIONS

Bing-Ze Lu^{*} and Richard Tsai[†]

ABSTRACT

We develop a multilevel stochastic-gradient neural solver for boundary integral equations of the second kind. The unknown density is represented by a multilayer perceptron, trained by minimizing the Nyström-discretized residual on a ladder of refining quadrature grids, each level warm-started from the parameters of the previous one. Each step requires only dense matrix-vector products on mini-batches of collocation rows and network passes, operations that map directly onto GPU hardware. The residual contraction is governed by the empirical neural tangent kernel (NTK), the discrete sample of a single continuum kernel. On a fixed grid, training stalls once the residual concentrates in modes the network contracts slowly, the plateau described by the frequency principle; a spectral analysis explains, and experiments confirm, how refining the quadrature resolves more of the continuum kernel's spectrum and returns these modes to the optimizer's reach. Spectral bias, elsewhere an obstruction to neural network solvers, thus serves as the smoother of a multigrid-type iteration, with quadrature refinement in place of coarse-grid correction. Under a uniform regularity bound on the network, the total work is a constant multiple of the work on the finest grid, and the uniform conditioning of the discrete second-kind operator leaves the NTK as the sole rate-determining spectrum while converting the training residual into an a posteriori error bound. Experiments on interior Dirichlet Laplace/Poisson problems and exterior Neumann Helmholtz problems, using both parametric and signed-distance surface representations, demonstrate the effectiveness and efficiency of the proposed method compared with GMRES at comparable tolerances.

Keywords Boundary integral equations, implicit boundary integral method, multilevel training, neural network solvers, stochastic optimization, neural tangent kernel

1 Introduction

This paper develops a GPU-friendly multilevel algorithm for solving a class of dense linear systems that arise from the discretization of boundary integral equations (BIEs). The unknown density on the boundary is represented by a multilayer perceptron (MLP), and the algorithm trains the network through residual minimization on a sequence of progressively refined quadrature grids.

^{*}Department of Mathematics, National Chung Cheng University, Minhsiung, Chiayi 100190, Taiwan. bingzelu.math@gmail.com

[†]Department of Mathematics and Oden Institute for Computational Engineering and Sciences, The University of Texas at Austin, Austin, Texas 78712, U.S.A. ytsai@math.utexas.edu

Let $\Omega \subset \mathbb{R}^d$, $d = 2, 3$, be a bounded domain with C^2 boundary $\Gamma = \partial\Omega$. We consider Fredholm integral equations of the second kind posed on Γ ,

$$\mathcal{A}\rho := \frac{1}{2}\rho + \mathcal{K}\rho = g, \quad (\mathcal{K}\rho)(x) := \int_{\Gamma} k(x, y) \rho(y) dS(y), \quad x \in \Gamma, \quad (1)$$

where $\rho : \Gamma \rightarrow \mathbb{C}$ is the unknown density, $g \in H^{1/2}(\Gamma)$ is prescribed boundary data, and \mathcal{K} is a compact integral operator on $L^2(\Gamma)$ (or, under appropriate regularity, on $C(\Gamma)$). The kernel k is determined by the underlying problem.

Equations of the form (1) can be derived from elliptic boundary value problems posed on Ω or on the exterior $\bar{\Omega}^c$ [14, 8]. A representative pair of examples is the Laplace equation with Dirichlet data on Ω and the exterior Helmholtz problem with Neumann data on $\bar{\Omega}^c$. The $\frac{1}{2}$ in (1) is the canonical jump term for the interior-Dirichlet double-layer reformulation; the analysis below is invariant under the sign of the jump and applies equally to formulations in which $-\frac{1}{2}\rho$ appears in place of $+\frac{1}{2}\rho$. In each case, the PDE solution admits a layer potential representation

$$u(x) = \int_{\Gamma} \tilde{k}(x, y) \rho(y) dS(y), \quad x \in \mathbb{R}^d \setminus \Gamma, \quad (2)$$

in which \tilde{k} is a (possibly different) kernel built from the fundamental solution of the underlying differential operator. The solution procedure splits into two stages. First, one solves the BIE (1) for the density ρ on Γ . Second, the PDE solution at any point x off the surface is recovered by evaluating the integral (2).

One of the notable properties of this formulation is the conditioning of \mathcal{A} . The compactness of \mathcal{K} on $L^2(\Gamma)$ implies that the spectrum of $\mathcal{A} = \frac{1}{2}\mathcal{I} + \mathcal{K}$ accumulates at $\frac{1}{2}$ and is bounded away from 0 whenever $0 \notin \sigma(\mathcal{A})$. The operator \mathcal{A} is therefore well-conditioned, and the same uniform conditioning is inherited by reasonable discretizations of it.

The discretized system of linear equation $A_N \rho_N = g_N$, with $A_N = \frac{1}{2}I + K_N \in \mathbb{C}^{N \times N}$, is solved typically by an iterative solver. The kernel k in classical BIE formulations is generally weakly singular at $y = x$ and bounded with prescribed decay away from the diagonal, so the matrix A_N is dense; for problems of practical size in three dimensions ($N \gtrsim 10^5$) the cost of forming and applying A_N dominates the solver. Because A_N is well-conditioned, GMRES [17] converges in a number of iterations bounded independently of N once the spectrum has stabilized, but each iteration requires a matrix-vector product against the dense A_N at $\mathcal{O}(N^2)$ cost. Hierarchical compression of the far-field interaction, by the Fast Multipole Method [9, 7] or the \mathcal{H} -matrix frameworks [11], brings this cost down to $\mathcal{O}(N \log N)$ or $\mathcal{O}(N)$.

This work explores a complementary design point: an algorithm that represents the BIE solution with neural networks and leverages GPU parallelism to reduce computational cost. The density is parametrized by a multilayer perceptron ρ_{θ} with parameters $\theta \in \mathbb{R}^p$, determined by minimizing the discrete BIE residual on a sequence of progressively refined quadrature grids. Each level inherits θ from the previous one as its initial condition, so the network warm-starts from a representation already accurate on the coarser grid and need only resolve the additional content, the finer quadrature exposes.

This algorithmic structure is suited to second-kind BIEs by a structural feature of the operator. The compactness of \mathcal{K} that uniformly bounds $\kappa(A_N)$ collapses the BIE-side spectrum to a bounded multiplicative factor in the residual-flow analysis, leaving the empirical NTK $T_{\theta, N} = J_{\theta, N} J_{\theta, N}^*$ as the operative quantity governing per-mode contraction. $T_{\theta, N}$ is the W -weighted realization on the chosen grid of a single continuum kernel \mathcal{T}_{θ} . Refining the grid resolves more of \mathcal{T}_{θ} 's spectrum at the current θ , while the training at each level raises the contraction rates of the modes still carrying residual; the band of modes the scheme contracts, therefore widens as it climbs the grid hierarchy. This coupling of spectral resolution with the training dynamics is the feature on which the analysis of Section 3 rests.

This mechanism addresses a documented obstruction to neural network solvers. The frequency principle [16, 19] reports that gradient-based training fits low-frequency content first, and that high-frequency components of the residual contract slowly, often failing to converge within practical budgets; our experiments on a single fine grid reproduce exactly this plateau. The multilevel schedule circumvents it. At each level, the same spectral bias that causes the plateau damps the modes that level resolves, playing the role the smoother plays in multigrid, while refinement re-exposes the content training could not previously reach. The spectral properties of second-kind integral operators add a further favorable ingredient: because the spectrum of \mathcal{A} is bounded above and below away from zero, the BIE contributes only a bounded factor to the per-mode contraction rate, and the leading NTK eigenvalues translate directly into fast residual decay. The NTK is the only spectrum the optimizer must contend with. Section 4.1 documents the single-level plateau and its removal by the multilevel schedule.

The proposed algorithm is, on its own, a fast BIE solver designed for GPU hardware. When higher accuracy is required, the trained network admits a natural pairing with a classical iterative solver: the continuous density it produces serves as a high-quality initial guess that drives the classical solver to near machine-epsilon accuracy in a small number of additional iterations.

The remainder of the paper is organized as follows. Section 2 reviews the Nyström discretization of (1), the least-squares residual functionals at continuum and discrete levels, and the gradient flow analysis of these functionals on both the density and the network parameters. Section 3 introduces the multilevel stochastic-gradient neural solver and develops the spectral picture that motivates it. Section 4 reports numerical experiments on an interior Dirichlet Laplace/Poisson problem and an exterior Neumann Helmholtz problem, under both parametric and volumetric representations of the surface.

2 Preliminaries

2.1 Notation

Throughout, $\Omega \subset \mathbb{R}^d$, $d \in \{2, 3\}$, is a bounded domain with C^2 boundary $\Gamma = \partial\Omega$, equipped with the surface measure dS . Function spaces over Γ are written without ambient brackets: $L^2(\Gamma)$, $C(\Gamma)$, $H^s(\Gamma)$, with the L^2 inner product $\langle u, v \rangle_{L^2(\Gamma)} := \int_{\Gamma} u(y) v(y) dS(y)$.

Surface and quadrature. $\Gamma_N := \{x_1, \dots, x_N\} \subset \Gamma$ denotes a set of N quadrature points on Γ , with associated positive weights $\{w_1, \dots, w_N\}$, $w_j > 0$. The quadrature rule $Q_N(f) := \sum_{j=1}^N w_j f(x_j)$ approximates the surface integral $\int_{\Gamma} f dS$ for continuous integrands f . We collect the weights into the diagonal matrix $W := \text{diag}(w_1, \dots, w_N) \in \mathbb{R}^{N \times N}$.

Weighted inner product and adjoints on \mathbb{R}^N . We endow \mathbb{R}^N with the discrete weighted inner product

$$\langle u, v \rangle_W := \sum_{j=1}^N w_j u_j v_j = v^\top W u, \quad u, v \in \mathbb{R}^N, \quad (3)$$

which is the natural quadrature image of the $L^2(\Gamma)$ inner product. Because the quadrature weights are positive, $\langle \cdot, \cdot \rangle_W$ is positive definite and defines a genuine inner product on \mathbb{R}^N . The adjoint of an operator $T \in \mathbb{R}^{N \times N}$ with respect to (3) is $T^* = W^{-1} T^\top W$.

Restriction operator. The restriction operator

$$\Pi_{\Gamma_N} : C(\Gamma) \longrightarrow \mathbb{R}^N, \quad \Pi_{\Gamma_N}[\rho]_j := \rho(x_j), \quad j = 1, \dots, N,$$

maps a continuous function on Γ to its values at the quadrature nodes.

Densities. $\rho: \Gamma \rightarrow \mathbb{R}$ denotes a continuous (typically C^1) density on Γ , and $\rho_N := \Pi_{\Gamma_N}[\rho] \in \mathbb{R}^N$ its discretization. The exact solution of (1) is denoted ρ^* , with discretization ρ_N^* .

Operators. We use calligraphic font for operators acting on function spaces over Γ and ordinary math font for their finite-dimensional discretizations: \mathcal{A}, \mathcal{K} are the continuum BIE and integral operators in (1); A_N, K_N are the corresponding $N \times N$ matrices. Adjoints in $L^2(\Gamma)$ are denoted $\mathcal{A}^*, \mathcal{K}^*$. We reserve the asterisk $*$ for adjoints throughout, and the star \star for exact or optimal quantities (densities and parameters); the two symbols are kept visually distinct on purpose.

Restriction to real-valued densities. The analysis in this section and the next treats real-valued densities and operators. The extension to $\rho: \Gamma \rightarrow \mathbb{C}$, required for the Helmholtz problems of Section 4, follows by realification: identify $\mathbb{C} \cong \mathbb{R}^2$ and apply the same arguments to the resulting $2N$ -dimensional real system. The convergence of the discretization, the second-kind spectral structure, and the spectral analysis of the parameter and residual flows all carry over with A_N replaced by its realification.

2.2 The Nyström method

Applying the quadrature rule Q_N to the integral operator \mathcal{K} in (1) produces the Nyström operator

$$(K_N \phi)_i := \sum_{j=1}^N w_j k(x_i, x_j) \phi_j, \quad i = 1, \dots, N, \quad (4)$$

acting on $\phi \in \mathbb{R}^N$, and the discrete BIE operator

$$A_N := \frac{1}{2}I + K_N \in \mathbb{R}^{N \times N}. \quad (5)$$

Setting $\rho_N = \Pi_{\Gamma_N}[\rho^*]$ and $g_N = \Pi_{\Gamma_N}[g]$, the Nyström discretization of (1) is the linear system

$$A_N \rho_N = g_N. \quad (6)$$

When dealing with singular kernels, we assume that the chosen quadrature provides a convergent approximation. Typically this involves regularizing the kernel near $x = y$. For notational simplicity, we will simply write $k(x, y)$.

Consistency, invertibility, and spectral convergence. The classical Nyström theory of [1, 3] provides the properties of A_N that drive the analysis below. Under the hypotheses that k is continuous (or weakly singular with appropriate regularization) and the quadrature rule $\{Q_N\}$ converges pointwise on $C(\Gamma)$:

1. the family $\{K_N\}$ is collectively compact, and $K_N \rightarrow \mathcal{K}$ pointwise on $C(\Gamma)$;
2. A_N is invertible for all N sufficiently large, and $\|A_N^{-1}\|$ is uniformly bounded in N (in the sup-norm, and hence in the W -norm for quasi-uniform quadrature);
3. the nonzero eigenvalues of A_N converge to the nonzero eigenvalues of \mathcal{A} , and the corresponding spectral projectors converge in operator norm. If the kernel is C^ν away from the diagonal and the quadrature is of order ν , then for any nonzero eigenvalue μ of \mathcal{A} isolated from the rest of $\sigma(\mathcal{A})$, the perturbation $|\mu^{(N)} - \mu|$ and the projector deviation are $\mathcal{O}(h^\nu)$, where h is the quadrature spacing.

The qualitative consequence is that the spectrum of A_N accumulates near $\frac{1}{2}$, is bounded away from 0 uniformly in N once N is large enough, and is bounded above. The condition number $\kappa(A_N)$ is therefore $\mathcal{O}(1)$ in N .

Convergence of the discrete solution. A consequence is the standard discretization error estimate

$$\|\Pi_{\Gamma_N}[\rho^*] - \rho_N^*\|_W \leq C h^\nu, \quad (7)$$

where ρ^* solves (1), ρ_N^* solves (6), h is the characteristic quadrature spacing, and C depends on the regularity of ρ^* and on the order ν of the quadrature.

2.3 Least-squares residual functionals

Our solver determines an approximate density by minimizing the L^2 -residual of the BIE (1), evaluated either continuously on Γ or discretely through the quadrature.

Continuum loss. For $\rho \in L^2(\Gamma)$ define the continuum residual

$$r[\rho](x) := (\mathcal{A}\rho)(x) - g(x), \quad x \in \Gamma, \quad (8)$$

and the continuum least-squares functional

$$\mathcal{L}[\rho; \Gamma] := \frac{1}{2} \int_{\Gamma} |r[\rho](x)|^2 dS(x) = \frac{1}{2} \|\mathcal{A}\rho - g\|_{L^2(\Gamma)}^2. \quad (9)$$

Discrete loss. For $\rho_N \in \mathbb{R}^N$ define the discrete residual

$$r_N[\rho_N] := A_N \rho_N - g_N \in \mathbb{R}^N, \quad (10)$$

and the discrete least-squares functional

$$L(\rho_N; \Gamma_N) := \frac{1}{2} \sum_{j=1}^N w_j |r_N[\rho_N]_j|^2 = \frac{1}{2} \langle r_N[\rho_N], r_N[\rho_N] \rangle_W. \quad (11)$$

$L(\cdot; \Gamma_N)$ is the quadrature image of $\mathcal{L}[\cdot; \Gamma]$ when the input is the restriction of a continuous density.

Convexity and uniqueness. Both functionals are convex quadratic in their respective arguments. The gradient of $\mathcal{L}[\cdot; \Gamma]$ with respect to $\rho \in L^2(\Gamma)$ is

$$\nabla_{\rho} \mathcal{L}[\rho; \Gamma] = \mathcal{A}^*(\mathcal{A}\rho - g), \quad (12)$$

and the gradient of $L(\cdot; \Gamma_N)$ with respect to $\rho_N \in \mathbb{R}^N$ in the W -weighted inner product is

$$\nabla_{\rho_N} L(\rho_N; \Gamma_N) = A_N^*(A_N \rho_N - g_N), \quad (13)$$

where A_N^* is the W -adjoint introduced after (3).

The first-order condition for a minimizer reads $\mathcal{A}^* \mathcal{A} \rho = \mathcal{A}^* g$ at the continuum. Since $0 \notin \sigma(\mathcal{A})$, the operator $\mathcal{A}^* \mathcal{A}$ is positive definite on $L^2(\Gamma)$ with spectrum bounded away from 0, and $\mathcal{L}[\cdot; \Gamma]$ admits the unique global minimizer $\rho^* = \mathcal{A}^{-1} g$, at which $\mathcal{L}[\rho^*; \Gamma] = 0$. Classical theory establishes a similar picture for the discretized setting: for sufficiently large N , A_N is invertible, and $L(\cdot; \Gamma_N)$ admits the unique global minimizer $\rho_N^* = A_N^{-1} g_N$ with $L(\rho_N^*; \Gamma_N) = 0$.

Network parametrization, parametrized loss, and residual. The unknown density on Γ is represented by a multilayer perceptron (MLP) $\rho_\theta: \Gamma \rightarrow \mathbb{R}$ with trainable parameters $\theta \in \mathbb{R}^p$, and we write

$$\rho_{\theta,N} := \Pi_{\Gamma_N}[\rho_\theta] \in \mathbb{R}^N \quad (14)$$

for its quadrature sample. The concrete architectural choices depend on how Γ is described in the application and are deferred to Section 4; the analysis of this section applies to any such parametrization. The loss functionals (9) and (11) pull back through the parametrization to functions of θ ,

$$L(\theta; \Gamma) := \mathcal{L}[\rho_\theta; \Gamma], \quad L(\theta; \Gamma_N) := L(\rho_{\theta,N}; \Gamma_N), \quad (15)$$

and the corresponding residuals are

$$r_\theta := \mathcal{A}\rho_\theta - g \in L^2(\Gamma), \quad r_{\theta,N} := A_N \rho_{\theta,N} - g_N \in \mathbb{R}^N. \quad (16)$$

Although $\mathcal{L}[\cdot; \Gamma]$ and $L(\cdot; \Gamma_N)$ are convex in their direct arguments, the composition with the nonlinear map $\theta \mapsto \rho_\theta$ generally destroys convexity, so $L(\theta; \Gamma)$ and $L(\theta; \Gamma_N)$ are not convex in θ . The remainder of the section studies the geometry of these landscapes and the dynamics of the parameter flow on them.

2.4 Gradient flows

We record the dynamics of the gradient flows on \mathcal{L} and L . We begin with the unparametrized flows on the density itself; these serve as the reference dynamics against which the parameter-space flow, introduced afterwards, is compared. The parameter-space flow is the one the solver actually realizes, and the operator that acts as its preconditioner, the neural tangent kernel, is identified along the way.

Reference gradient flows. The $L^2(\Gamma)$ gradient flow of $\mathcal{L}[\cdot; \Gamma]$ is

$$\frac{d}{dt}\rho = -\mathcal{A}^*(\mathcal{A}\rho - g), \quad (17)$$

and the W -weighted gradient flow of $L(\cdot; \Gamma_N)$ on \mathbb{R}^N is

$$\frac{d}{dt}\rho_N = -A_N^*(A_N\rho_N - g_N). \quad (18)$$

Since $\mathcal{A} = \frac{1}{2}\mathcal{I} + \mathcal{K}$ has spectrum bounded above and below away from 0, $\mathcal{A}^*\mathcal{A}$ has spectrum bounded above and below by positive constants. By Section 2.2, the spectrum of A_N accumulates near $\frac{1}{2}$, so that of $A_N^*A_N$ accumulates near $|\frac{1}{2}|^2 = \frac{1}{4}$ and is bounded above and below uniformly in N . Both reference flows therefore contract the loss exponentially at a rate independent of the discretization.

Parameter-space flow. The gradient flow on the parameters reads

$$\frac{d}{dt}\theta = -\nabla_\theta L(\theta; \Gamma) \quad (\text{continuum}), \quad \frac{d}{dt}\theta = -\nabla_\theta L(\theta; \Gamma_N) \quad (\text{discrete}). \quad (19)$$

The analysis below is relevant to standard gradient-based optimization methods. The continuum and discrete cases of (19) are parallel: we develop the continuum picture in detail and then state its discrete counterpart.

Applying the chain rule componentwise to $L(\theta; \Gamma) = \mathcal{L}[\rho_\theta; \Gamma]$ writes each parameter-gradient component as an $L^2(\Gamma)$ inner product of the density-side residual gradient \mathcal{A}^*r_θ with the network's parameter sensitivity,

$$(\nabla_\theta L(\theta; \Gamma))_k = \left\langle \mathcal{A}^*r_\theta, \frac{\partial \rho_\theta}{\partial \theta_k} \right\rangle_{L^2(\Gamma)}, \quad k = 1, \dots, p. \quad (20)$$

The sensitivity vectors $\{\partial\rho_\theta/\partial\theta_k\}_{k=1}^p$ span the *neural tangent space* at θ in $L^2(\Gamma)$.

Pulling (19) back to the density via the chain rule gives the induced dynamics for ρ_θ :

$$\frac{d}{dt}\rho_\theta(x) = \sum_{k=1}^p \partial_{\theta_k}\rho_\theta(x) \frac{d}{dt}\theta_k = - \int_{\Gamma} T_\theta(x, y) \mathcal{A}^*(\mathcal{A}\rho_\theta - g)(y) dS(y), \quad (21)$$

where

$$T_\theta(x, y) := \langle \nabla_\theta \rho_\theta(x), \nabla_\theta \rho_\theta(y) \rangle_{\mathbb{R}^p} = \sum_{k=1}^p \partial_{\theta_k}\rho_\theta(x) \partial_{\theta_k}\rho_\theta(y) \quad (22)$$

is the *neural tangent kernel function* associated with ρ_θ . The corresponding integral operator on $L^2(\Gamma)$ is

$$(\mathcal{T}_\theta u)(x) := \int_{\Gamma} T_\theta(x, y) u(y) dS(y). \quad (23)$$

Substituting (22) into the right-hand side and exchanging the integral with the finite sum gives the factorization

$$(\mathcal{T}_\theta u)(x) = \sum_{k=1}^p \langle \partial_{\theta_k}\rho_\theta, u \rangle_{L^2(\Gamma)} \partial_{\theta_k}\rho_\theta(x), \quad u \in L^2(\Gamma), \quad (24)$$

from which several properties of \mathcal{T}_θ follow directly. The range of \mathcal{T}_θ lies in $\text{span}\{\partial_{\theta_k}\rho_\theta\}_{k=1}^p$, a subspace of dimension at most p . Cauchy–Schwarz on each inner product gives $\|\mathcal{T}_\theta u\|_{L^2(\Gamma)} \leq (\sum_{k=1}^p \|\partial_{\theta_k}\rho_\theta\|_{L^2(\Gamma)}^2) \|u\|_{L^2(\Gamma)}$, so \mathcal{T}_θ is bounded. Pairing (24) against $v \in L^2(\Gamma)$,

$$\langle \mathcal{T}_\theta u, v \rangle_{L^2(\Gamma)} = \sum_{k=1}^p \langle \partial_{\theta_k}\rho_\theta, u \rangle_{L^2(\Gamma)} \langle \partial_{\theta_k}\rho_\theta, v \rangle_{L^2(\Gamma)},$$

which is symmetric in (u, v) and reduces to $\sum_{k=1}^p \langle \partial_{\theta_k}\rho_\theta, u \rangle_{L^2(\Gamma)}^2 \geq 0$ when $v = u$, so \mathcal{T}_θ is self-adjoint and positive semi-definite. Bounded subsets of the finite-dimensional range are precompact, hence \mathcal{T}_θ is compact on $L^2(\Gamma)$. We summarize:

Proposition 2.1 (Properties of the continuum NTK operator). *Let $\rho_\theta : \Gamma \rightarrow \mathbb{R}$ be a network parametrization with p trainable parameters whose sensitivities $\partial_{\theta_k}\rho_\theta$ are continuous on Γ . Then the NTK integral operator $\mathcal{T}_\theta : L^2(\Gamma) \rightarrow L^2(\Gamma)$ defined by (23) is bounded, self-adjoint, positive semi-definite, and of rank at most p . In particular, \mathcal{T}_θ is compact on $L^2(\Gamma)$.*

The same calculation on Γ_N replaces the $L^2(\Gamma)$ pairing by the W -pairing and the operator \mathcal{A}^* by its W -adjoint A_N^* :

$$(\nabla_\theta L(\theta; \Gamma_N))_k = \left\langle A_N^* r_{\theta, N}, \frac{\partial \rho_{\theta, N}}{\partial \theta_k} \right\rangle_W, \quad k = 1, \dots, p, \quad (25)$$

or equivalently

$$\nabla_\theta L(\theta; \Gamma_N) = J_{\theta, N}^* A_N^* r_{\theta, N}, \quad (26)$$

where $J_{\theta, N}$ is the Jacobian

$$J_{\theta, N} \in \mathbb{R}^{N \times p}, \quad (J_{\theta, N})_{i, k} := \partial_{\theta_k}\rho_\theta(x_i). \quad (27)$$

The induced flow on the sampled density is

$$\frac{d}{dt}\rho_{\theta, N} = J_{\theta, N} \frac{d}{dt}\theta = -T_{\theta, N} A_N^*(A_N \rho_{\theta, N} - g_N), \quad (28)$$

with the *empirical neural tangent kernel* on Γ_N

$$T_{\theta,N} := J_{\theta,N} J_{\theta,N}^* \in \mathbb{R}^{N \times N}. \quad (29)$$

Writing G_N for the Gram matrix $(G_N)_{ij} = T_{\theta}(x_i, x_j) = \langle \nabla_{\theta} \rho_{\theta}(x_i), \nabla_{\theta} \rho_{\theta}(x_j) \rangle_{\mathbb{R}^p}$, the empirical NTK is the W -weighted realization $T_{\theta,N} = G_N W$ of \mathcal{T}_{θ} on Γ_N (the weight factor distinguishes it from the symmetric Gram matrix G_N). The same argument as in the proof of Proposition 2.1, applied to the factorization $T_{\theta,N} = J_{\theta,N} J_{\theta,N}^*$, shows that $T_{\theta,N}$ is W -self-adjoint, positive semi-definite on $(\mathbb{R}^N, \langle \cdot, \cdot \rangle_W)$, and of rank at most $\min(p, N)$. It is rank-deficient whenever $p < N$, the regime of interest at the finer levels.

Comparison with the un-parametrized flow. The reference flows (17) and (18) correspond formally to $T_{\theta}(x, y) = \delta(x - y)$ (equivalently $\mathcal{T}_{\theta} = \mathcal{I}$, $T_{\theta,N} = I$). Because $A_N^* A_N$ is uniformly well-conditioned in N (Section 2.2), every component of the density error $\rho_N - \rho_N^*$ contracts at a rate bounded uniformly in N . For a general θ , \mathcal{T}_{θ} is compact and $T_{\theta,N}$ is rank-deficient, with spectra accumulating at 0; the parametrized flow (28) carries $T_{\theta,N}$ as its leading factor, so the instantaneous velocity of $\rho_{\theta,N}$ lies in $\text{range}(T_{\theta,N})$ and is small on directions where $T_{\theta,N}$ has small eigenvalues. The network’s own kernel structure thus becomes a source of slow components in the dynamics. The dependence on the NTK spectrum is specific to plain parameter gradient descent: the so-called natural gradient, which preconditions the parameter update by the inverse Gram matrix of the sensitivities $\{\partial_{\theta_k} \rho_{\theta}\}_{k=1}^p$, would replace \mathcal{T}_{θ} in (21) by the orthogonal projection onto the neural tangent space and recover uniform decay within that space, at the cost of solving a $p \times p$ linear system at every step. Section 3 develops this picture as the basis for the multilevel strategy.

Residual dynamics. Applying A_N to (28) yields the residual flow

$$\frac{d}{dt} r_{\theta,N} = -A_N T_{\theta,N} A_N^* r_{\theta,N}. \quad (30)$$

The driving operator $A_N T_{\theta,N} A_N^*$ is W -self-adjoint and positive semi-definite.

The gradient flow (30) drives $\|r_{\theta,N}\|_W$ to 0 only as $t \rightarrow \infty$. It also gives us hints about the *rate* at which $\|r_{\theta,N}\|_W$ contracts along the parameter-space gradient flow. The presence of the empirical NTK $T_{\theta,N}$ in the driving operator $A_N T_{\theta,N} A_N^*$ is a first indication that the spectrum of $T_{\theta,N}$ shapes this contraction, a subject we develop in Section 3.

In practice, training has to stop at finite time, and one needs a quantitative bound on the resulting error in terms of an observable quantity. The well-conditioning of A_N from Section 2.2 provides such an a posteriori estimate through the residual.

Lemma 2.1 (Residual controls error). *Let N be large enough that A_N is invertible. For every $\rho_N \in \mathbb{R}^N$,*

$$\|\rho_N - \rho_N^*\|_W \leq \|A_N^{-1}\|_W \|A_N \rho_N - g_N\|_W, \quad (31)$$

and the constant $\|A_N^{-1}\|_W$ is bounded uniformly in N by the Nyström theory of Section 2.2. In particular, applied to the network sample $\rho_{\theta,N} := \Pi_{\Gamma_N}[\rho_{\theta}]$, the inequality controls $\|\rho_{\theta,N} - \rho_N^\|_W$ by $\|r_{\theta,N}\|_W$.*

3 The multilevel stochastic-gradient neural solver

With the discretization, the residual loss, and the parameter-space gradient flow in place, we now turn to the solver itself: a multilevel stochastic-gradient minimization of the discrete residual loss over a ladder of refining quadratures $N_1 < N_2 < \dots < N_L$. The levels are visited in an order fixed by a schedule, each stage warm-started from the parameters returned by the previous one. We consider two such schedules: a

progressive one, which traverses the ladder once from coarse to fine, and a *cyclic* one, which interleaves refinement with returns to coarser grids.

Sections 3.1–3.3 give the rationale for this design: a computational accounting on GPU hardware, a correspondence with multigrid in which spectral bias plays the role of the smoother, and the spectral dynamics by which the effective tangent space expands across levels. Sections 3.4–3.5 then set up the grid ladder and its visiting schedules, state the algorithm in pseudocode, and explain the effects of warm-starting the training at each new level.

3.1 Computational accounting

We work on algorithms under two design choices. The unknown density is a neural network ρ_θ , optimized by gradient-based methods on the discrete residual loss (11) with stochastic mini-batches of quadrature points. The dense matrix A_N is applied directly, without FMM-style hierarchical compression. Both choices place the solver at a formal disadvantage relative to a contemporary BIE solver.

On a well-conditioned second-kind system, GMRES [17] converges in a number of iterations bounded independently of N once the discrete spectrum has stabilized, and across a Krylov subspace of fixed dimension it delivers the minimum-residual iterate. A first-order gradient method on the residual loss is bounded above by this property at equal subspace dimension; the gap is real even before the network parametrization is folded in. Separately, the per-iteration arithmetic of a dense matrix-vector product against A_N is $\mathcal{O}(N^2)$, whereas FMM-accelerated GMRES achieves $\mathcal{O}(N \log N)$ or $\mathcal{O}(N)$ [9, 7].

We forgo this acceleration and accept the quadratic arithmetic in exchange for a computational pattern built entirely from dense, uniform operations that the GPU executes near its peak. Instead, we aim at taking advantage of four specific features:

(i) *Dense and uniform per-iteration kernels.* Each step is a dense matrix-vector product against A_N , a pointwise residual evaluation, and a backward pass through the network.

(ii) *Mini-batches reduce the per-step cost.* A stochastic gradient of $L(\theta; \Gamma_N)$ formed from b collocation rows requires only the corresponding b rows of A_N . The per-step arithmetic drops from $\mathcal{O}(N^2)$ to $\mathcal{O}(bN)$. On a GPU with sufficient parallelism, the wall-clock per step is set by the $\mathcal{O}(\log N)$ depth of the dot-product reductions and the bandwidth needed to stream the bN kernel entries; when this slice fits in high-bandwidth memory, it is essentially independent of N in the practical range. The algorithm tolerates any $b \in \{1, \dots, N\}$.

(iii) *The network is a function on Γ (or its embedding), not a grid function.* Refining or coarsening the quadrature changes only the points at which the loss is evaluated; the same network serves at every level. A mesh-based multigrid scheme requires explicit prolongation and restriction operators between levels, the design of which is a substantive part of the method; here no such operators are needed.

(iv) *Warm starts amortize the per-level work.* Because one sufficiently expressive network represents the solution at every level, we can minimize a sequence of quadrature losses, each one initialized from the network already optimized at a neighboring level rather than trained from scratch.

An approximation that is already accurate at one resolution is corrected for the error components exposed by the refined quadrature. This way, the effort required at a finer level is far less than training directly at that level from a random initialization.

The order in which the levels are visited is itself a design choice, developed in Section 3.4.

3.2 Spectral bias and the effective neural tangent space

The efficiency of a multilevel solver may depend on the spectral bias in the solver’s iterative procedures. The classical instance is geometric multigrid for PDEs [10], whose relaxation sweep damps the high-frequency components of the error substantially faster than the low-frequency ones. The slowly-damped, low-frequency error that remains is well represented on a coarser grid, where it is corrected at a fraction of the cost. Letting each level resolve only the band of error it handles most cheaply, rather than resolving every scale on the finest grid, bounds the total work by a small multiple of a single fine-grid sweep.

The proposed algorithm is a variant of this construction, enabled by items (iii) and (iv) of §3.1. Specifically, we replace the relaxation step with a stochastic gradient optimizer (Adam [13]), substitute the coarse-grid correction with quadrature refinement, and, to complete the analogy, we can identify the identity map on θ as the prolongation between levels (since the network is a function on Γ rather than a discrete grid function). We refer to the resulting procedure as the *multilevel stochastic-gradient neural solver* (MLSG). Whether the analogy is more than superficial hinges on the smoother. We shall argue, by analyzing the induced gradient flows, that a gradient-based optimizer on (11) composed with a network parametrization has the spectral bias the analogy requires.

The contraction rate of the residual flow (30) is governed by the spectrum of the driving operator $A_N T_{\theta,N} A_N^*$. Because the factor $A_N^* A_N$ is uniformly well-conditioned (§2.4), the obstruction to fast training lies entirely in the empirical NTK $T_{\theta,N} = J_{\theta,N} J_{\theta,N}^*$ and how the residual aligns with its eigenmodes.

Spectral decompositions. On the BIE side, $A_N^* A_N$ is W -self-adjoint, with eigenvalues $\lambda_{1,N}, \dots, \lambda_{N,N}$ clustering near $\frac{1}{4}$. On the network side, the empirical NTK has the spectral decomposition

$$T_{\theta,N} = V_N \Sigma_N V_N^*, \quad \Sigma_N = \text{diag}(\sigma_{1,N}, \dots, \sigma_{N,N}), \quad (32)$$

ordered $\sigma_{1,N} \geq \sigma_{2,N} \geq \dots \geq 0$, with W -orthonormal eigenvectors $\tau_{j,N}$ (the columns of V_N). The continuum NTK \mathcal{T}_θ on $L^2(\Gamma)$ is compact, with eigenvalues $\sigma_j \rightarrow 0$ and eigenfunctions τ_j .

The two spectra exhibit fundamentally different behaviors. The eigenvalues $\lambda_{j,N}$ are uniformly bounded and lack a natural frequency interpretation, whereas the $\sigma_{j,N}$ possess a frequency hierarchy. Provided a smooth activation function is used, the network’s parameter sensitivities $\partial_{\theta_k} \rho_\theta(x)$ are inherently smooth. Consequently, the associated continuum NTK integral operator \mathcal{T}_θ acts as a low-pass filter on $L^2(\Gamma)$. This property forces a rapid decay of the spectrum: the largest eigenvalues correspond to the smoothest eigenfunctions, while highly oscillatory modes are damped into the vanishing spectral tail ($\sigma_j \rightarrow 0$). This structure transfers directly to the discrete empirical NTK $T_{\theta,N}$. Its leading eigenvectors $\tau_{j,N}$ are the least oscillatory on Γ_N , providing a rigorous basis for the spectral bias phenomenon in neural network training [16, 19]. Note that throughout this work, “low-frequency mode” refers to a small index j (associated with a large $\sigma_{j,N}$), while “high-frequency” refers to a large j .

Loss decay and the effective tangent space. Project $A_N^* r_{\theta,N}$ onto the NTK eigenbasis,

$$A_N^* r_{\theta,N} = \sum_{j=1}^N \eta_j(t) \tau_{j,N}(\theta(t)), \quad \eta_j(t) := \langle \tau_{j,N}(\theta(t)), A_N^* r_{\theta,N}(t) \rangle_W. \quad (33)$$

The discrete loss $L(\theta; \Gamma_N) = \frac{1}{2} \|r_{\theta,N}\|_W^2$ of (15) then evolves as

$$\frac{d}{dt} L(\theta(t); \Gamma_N) = -\langle A_N^* r_{\theta,N}, T_{\theta,N} A_N^* r_{\theta,N} \rangle_W = -\sum_{j=1}^N \sigma_{j,N}(\theta) |\eta_j(t)|^2. \quad (34)$$

Compare this against the un-parametrized L^2 gradient flow (18), which acts on all of \mathbb{R}^N and contracts the loss at $\frac{d}{dt}L = -\|A_N^* r_{\theta,N}\|_W^2$: the reference case $T_{\theta,N} = I$, in which every direction is an eigendirection with $\sigma_{j,N} \equiv 1$. Read against this reference, (34) applies $T_{\theta,N}$ as a preconditioner: the j -th eigendirection contributes $\sigma_{j,N}(\theta) |\eta_j|^2$ in place of $|\eta_j|^2$, so directions with $\sigma_{j,N}(\theta) > 1$ are contracted faster than the reference and those with $\sigma_{j,N}(\theta) < 1$ slower. Grouping the eigendirections with $\sigma_{j,N}(\theta) \geq 1$, which contract at least as fast as the reference, we define the *effective neural tangent space* at parameter θ by

$$\mathcal{E}_\theta := \text{span}\{ \tau_{j,N}(\theta) : \sigma_{j,N}(\theta) \geq 1 \}. \quad (35)$$

The decay rate in (34) is set jointly by the eigenvalue magnitudes $\sigma_{j,N}$ and by how $A_N^* r_{\theta,N}$ distributes across the eigenmodes through the coordinates η_j . Projection coordinates η_j supported on \mathcal{E}_θ drive the loss down at least as fast as the un-parametrized reference; those supported on the orthogonal complement drive it down more slowly, or not at all. In particular, a component nearly orthogonal to the neural tangent space falls where $\sigma_{j,N} \approx 0$ and barely moves L , however large its coordinate η_j . The space \mathcal{E}_θ is finite-dimensional (trivially, $\dim \mathcal{E}_\theta \leq \text{rank } T_{\theta,N} \leq \min(p, N)$) and, per the frequency reading above, consists of the less-oscillatory, low-mode eigenvectors $\tau_{j,N}$; in the continuum limit the analogous count $\#\{\sigma_j \geq 1\}$ is finite because $\sigma_j \rightarrow 0$.

The eigenpairs $(\sigma_{j,N}(\theta), \tau_{j,N}(\theta))$ evolve with $\theta(t)$ along the gradient flow (19), so (34) is the instantaneous loss derivative at the current $\theta(t)$, not a closed-form ODE for $L(\theta(t); \Gamma_N)$. We read it as the indicative spectral picture and revisit the time dependence numerically in the experiments.

3.3 Expansion of the effective neural tangent space

The effective tangent space does not stay fixed during training; it grows by two routes that together motivate a multilevel scheme. (a) Within a level, the residual drives the parameters and reshapes the empirical NTK, so \mathcal{E}_θ can enlarge by an amount set by the residual relative to the current spectrum; the rapid decay of $\sigma_{j,N}$ still confines it to a small leading band, and single-level training plateaus once the residual concentrates in modes that contract more slowly than the un-parametrized reference. (b) Across levels, refining the quadrature grid re-weights the loss so that error the coarse grid could not resolve reappears as significant residual, and the training that follows expands \mathcal{E}_θ over these newly exposed modes.

The within-level mechanism of (a) is visible in a one-hidden-layer reduction $\rho_\theta(x) = \sum_m a_m \psi(z_m(x))$, $z_m(x) = w_m^\top x + b_m$, whose empirical NTK separates into an amplitude-free block and amplitude-weighted blocks,

$$T_{\theta,N} = R + \sum_m a_m^2 G_m, \quad R = \sum_m \Psi_m \Psi_m^*, \quad G_m = \Phi_m \Phi_m^*, \quad (36)$$

where $\Psi_m = \Pi_{\Gamma_N}[\psi(z_m)]$ is the sampled activation of neuron m , $\Phi_m = \Pi_{\Gamma_N}[\psi'(z_m) \tilde{x}]$ its sampled inner-weight sensitivity ($\tilde{x} = (x, 1)$), adjoints are taken in the W -pairing, and $R, G_m \succeq 0$. The block R comes from the output weights a_m and is independent of them; each G_m comes from the inner weights (w_m, b_m) and enters weighted by a_m^2 . The quadratic form inherits the split,

$$\langle u, T_{\theta,N} u \rangle_W = \langle u, R u \rangle_W + \sum_m a_m^2 \langle u, G_m u \rangle_W, \quad (37)$$

and is nondecreasing in each a_m^2 since $G_m \succeq 0$. The block R is inert under amplitude growth: it fixes the baseline \mathcal{E}_θ of (a) but cannot carry a mode across the threshold. The blocks G_m can: raising any a_m^2 leaves no $\sigma_{j,N}$ smaller and lifts them most in the direction Φ_m . Which amplitudes grow is set by the residual, since the output-weight gradient is the W -overlap of the back-projected residual with the neuron's activation,

$$\dot{a}_m = -\langle A_N^* r_{\theta,N}, \Psi_m \rangle_W. \quad (38)$$

The neurons amplified are thus those whose activation Ψ_m represents the current residual, while the direction in which amplification lifts the spectrum is the sensitivity Φ_m . How sharply that lift targets the residual the neuron responds to is set by the activation: since differentiation acts as $\widehat{\psi}'(\xi) = i\xi\widehat{\psi}(\xi)$ in the Fourier variable ξ , for a general smooth ψ the sensitivity is tilted toward higher frequencies than the activation, so Φ_m and Ψ_m share only the scale $|w_m|$ and not the exact band. The sinusoid is the exception: $\sin' = \cos$ preserves the frequency $|w_m|$ up to a phase, so the modes lifted are precisely those carrying the residual and the within-level expansion is at its sharpest. This is a first reason to prefer the sinusoidal activations adopted in Section 4. In either case, whether the expansion crosses the threshold depends on the initial spectrum: where the residual overlaps modes already near it, training carries them across.

The within-level growth eventually stalls, once the residual the loss can see is exhausted and what remains lies in modes the grid underweights. Refinement then enlarges \mathcal{E}_θ by a route of its own: the empirical NTK is a discrete sample of the continuum kernel \mathcal{T}_θ , so a denser grid resolves eigenmodes the coarse grid could not represent, filling \mathcal{E}_θ toward the ceiling $\#\{\sigma_j \geq 1\}$ that \mathcal{T}_θ fixes at the current θ . Refinement cannot raise that ceiling; only the parameter motion of (a), by moving θ , enlarges the continuum set $\{\sigma_j \geq 1\}$ itself, and only up to the network’s capacity, since \mathcal{T}_θ has rank at most p at every θ . The two combine through the warm start: each refinement re-exposes the off-grid, high-frequency residual and reprojects it onto the new, larger eigenbasis, and because every factor of \dot{a}_m is rebuilt on the finer grid (Section 3.4), the next level runs a fresh flow rather than a continuation of the previous one. The effective tangent space therefore advances in steps, refinement filling it to the current ceiling and training then lifting the ceiling in turn. We track only the amplitude-driven growth, which is monotone and explicit; the rotation of the Φ_m under the w_m -dynamics (an instance of the tangent-kernel alignment documented for feature-learning networks [2]) and, for deeper networks, the weighting of each layer by its downstream weights both require the full sensitivity of $T_{\theta,N}$ to θ .

A consequence of (a) and (b) not commonly noted for residual-minimization solvers is the improved smoothness of the trained ρ_θ . At a given residual tolerance, ρ_θ matches ρ_N^* at the Γ_N nodes but is assembled off-grid from the less-oscillatory eigenvectors $\tau_{j,N}$ in \mathcal{E}_θ ; content outside \mathcal{E}_θ is essentially untouched by training and stays near its small initial value. As training advances to finer levels and \mathcal{E}_θ extends to higher modes, ρ_θ gains expressive capacity in those directions while still being built from the smooth half of the spectrum at each level.

Together, items (i)–(iv) of Section 3.1 and the spectral picture (a)–(b) reconcile the $\mathcal{O}(N^2)$ per-iteration arithmetic accepted in (i)–(ii) with a fast overall solver: the multilevel schedule controls the *number* of finest-grid iterations, so total work is amortized across levels rather than concentrated at the finest one.

3.4 The multilevel algorithm

This subsection sets up the grid ladder and its visiting schedules, defines the per-level losses and their minimizers, states the algorithm, and describes what the solver sees between levels.

Ladder of quadrature grids. Fix levels $\ell = 1, \dots, L$. At level ℓ we apply the chosen quadrature rule on Γ with N_ℓ nodes and positive weights, with node set and weight matrix

$$\Gamma^\ell := \Gamma_{N_\ell} = \{x_1^\ell, \dots, x_{N_\ell}^\ell\}, \quad W^\ell := \text{diag}(w_1^\ell, \dots, w_{N_\ell}^\ell). \quad (39)$$

We do not assume the grids are nested. The levels are indexed by increasing resolution, $N_1 < N_2 < \dots < N_L$, with a typical ratio $N_{\ell+1} = 2N_\ell$; they form a fixed ladder of resolutions from which the solver draws. The order in which the solver visits these levels is a separate ingredient, specified by the schedule introduced below, and need not be monotone.

Per-level residual and loss. At level ℓ the discrete least-squares functional (11) is

$$L^{(\ell)}(\theta) := \frac{1}{2} \|A_{N_\ell} \Pi_{\Gamma^\ell}[\rho_\theta] - g_{N_\ell}\|_{W^\ell}^2, \quad (40)$$

with discrete residual and parameter Jacobian

$$r_\theta^{(\ell)} := A_{N_\ell} \Pi_{\Gamma^\ell}[\rho_\theta] - g_{N_\ell}, \quad (J_\theta^{(\ell)})_{ik} := \partial_{\theta_k} \rho_\theta(x_i^\ell). \quad (41)$$

The parameter-space gradient is

$$\nabla_\theta L^{(\ell)}(\theta) = (J_\theta^{(\ell)})^* A_{N_\ell}^* r_\theta^{(\ell)} \in \mathbb{R}^p, \quad (42)$$

where both $(J_\theta^{(\ell)})^*$ and $A_{N_\ell}^*$ denote W^ℓ -adjoints, in the sense of Section 2.1. The empirical NTK at level ℓ is $T_\theta^{(\ell)} := J_\theta^{(\ell)} (J_\theta^{(\ell)})^* \in \mathbb{R}^{N_\ell \times N_\ell}$.

Per-level minimizers. $L^{(\ell)}$ is convex in $\Pi_{\Gamma^\ell}[\rho_\theta]$ and bounded below by 0. When the network has enough capacity to interpolate the discrete solution $\rho_{N_\ell}^*$ at the N_ℓ nodes of Γ^ℓ , the lower bound is attained at some level- ℓ minimizer θ^* , and the corresponding network output satisfies

$$\Pi_{\Gamma^\ell}[\rho_{\theta^*}] = \rho_{N_\ell}^*. \quad (43)$$

$L^{(\ell)}$ pins ρ_θ only on Γ^ℓ , so the values of ρ_{θ^*} on $\Gamma \setminus \Gamma^\ell$ are unconstrained, and ρ_{θ^*} is in general not a minimizer of either $L^{(\ell+1)}$ or the continuum loss (9).

Warm-started traversal and visiting schedules. The solver visits the levels of the ladder in an order fixed in advance by a *schedule*

$$\mathcal{S} = (s_1, s_2, \dots, s_T), \quad s_t \in \{1, \dots, L\}, \quad (44)$$

a sequence of T stages, each naming the grid used at that stage. Stage t trains on Γ^{s_t} , warm-started from the parameters returned by the previous stage,

$$\theta^{(t, \text{init})} := \theta^{(t-1)}, \quad \theta^{(t)} \approx \arg \min_\theta L^{(s_t)}(\theta), \quad (45)$$

with $\theta^{(0)}$ a fresh random initialization and $\theta^{(t)}$ the parameter returned after a finite number of stochastic gradient steps. The schedule is the only ingredient that distinguishes the solver's two modes. In the *progressive* schedule the order is strictly increasing, $\mathcal{S} = (1, 2, \dots, L)$: each stage refines the grid, the stage index coincides with the level index (we then write $\theta^{(\ell)}$), and the ladder is traversed once from coarse to fine, for example $N_1, \dots, N_4 = 50, 100, 150, 200$; this is the direct analog of the cascadic multigrid iteration of Bornemann and Deuffhard [4]. In a *cyclic* schedule the order is not monotone but interleaves refinement with returns to coarser grids, for example $\mathcal{S} = (1, 2, 3, 4, 3, 4, 5)$, the analog of the full multigrid (FMG) cycle: the representation trained on a finer grid is carried back to a coarser one and re-refined, so that content re-exposed by coarsening is retrained before the next ascent. The progressive schedule is the special case with no descents. The per-stage loop, mini-batch construction, and stage-advancement rule are stated next, as Algorithms 1 and 2.

The MLSG is stated in two pieces. Algorithm 1, MINIRES, performs single-level mini-batch residual minimization on a fixed quadrature grid; Algorithm 2, the MLSG proper, is the multilevel driver that calls MINIRES on the grids named by the visiting schedule \mathcal{S} , in turn, each warm-started from the parameters returned by the previous stage (45).

Mini-batch loss. For a mini-batch $\mathcal{B} \subset \{1, \dots, N_\ell\}$ at level ℓ , the stochastic estimator of $L^{(\ell)}$ used by the optimizer is

$$L_{\mathcal{B}}^{(\ell)}(\theta) := \frac{1}{2|\mathcal{B}|} \sum_{i \in \mathcal{B}} w_i^\ell |r_{\theta,i}^{(\ell)}|^2. \quad (46)$$

Computing $\nabla_{\theta} L_{\mathcal{B}}^{(\ell)}$ requires only the $|\mathcal{B}|$ rows of A_{N_ℓ} indexed by \mathcal{B} , together with one forward and one backward pass of ρ_{θ} at the N_ℓ quadrature nodes, for a per-step arithmetic count of $\mathcal{O}(|\mathcal{B}| N_\ell)$.

Algorithm 1 MINIRES: single-level mini-batch residual minimization

Require: Inputs:

- Quadrature grid Γ_N with weight matrix W ; BIE matrix A_N and data g_N
- Network ρ_{θ} ; initial parameters θ^{init}
- Maximum epochs M ; batch size b
- Learning-rate schedule $\{\eta_m\}_{m=1}^M$
- Stopping tolerance ε

Ensure: Trained parameters θ^{out}

```

1:  $\theta \leftarrow \theta^{\text{init}}$ 
2: for  $m = 1, 2, \dots, M$  do
3:   Draw a uniform random permutation  $\pi$  of  $\{1, \dots, N\}$ 
4:   Set  $K \leftarrow \lceil N/b \rceil$ 
5:   for  $k = 1, 2, \dots, K$  do
6:      $\mathcal{B}_k \leftarrow \{\pi((k-1)b+1), \dots, \pi(\min(kb, N))\}$ 
7:      $\hat{g} \leftarrow \nabla_{\theta} L_{\mathcal{B}_k}(\theta)$ 
8:      $\theta \leftarrow \text{Adam}(\theta, \hat{g}; \eta_m)$ 
9:   end for
10:  if  $L(\theta; \Gamma_N) \leq \varepsilon$  then
11:    break
12:  end if
13: end for
14: return  $\theta^{\text{out}} \leftarrow \theta$ 

```

Algorithm 2 MLSG: multilevel stochastic-gradient neural solver

Require: Inputs:

- Grid ladder $\{(\Gamma^\ell, W^\ell, A_{N_\ell}, g_{N_\ell})\}_{\ell=1}^L$
- Visiting schedule $\mathcal{S} = (s_1, \dots, s_T)$ with $s_t \in \{1, \dots, L\}$
(progressive: $\mathcal{S} = (1, \dots, L)$; cyclic: non-monotone)
- Network ρ_{θ} ; initial parameters $\theta^{(0)}$
- Per-stage epoch budgets $\{M_t\}_{t=1}^T$; batch size b
- Per-stage learning-rate schedules $\{\{\eta_m^{(t)}\}_{m=1}^{M_t}\}_{t=1}^T$
- Per-stage tolerances $\{\varepsilon_t\}_{t=1}^T$

Ensure: Trained parameters $\theta^{(T)}$

```

1: for  $t = 1, 2, \dots, T$  do
2:    $\ell \leftarrow s_t$  ▷ grid visited at stage  $t$ 
3:    $\theta^{(t)} \leftarrow \text{MINIRES}(\Gamma^\ell, W^\ell, A_{N_\ell}, g_{N_\ell}, \rho_{\theta}, \theta^{(t-1)}, M_t, b, \{\eta_m^{(t)}\}_{m=1}^{M_t}, \varepsilon_t)$ 
4: end for
5: return  $\theta^{(T)}$ 

```

Tolerance schedule. By Lemma 2.1, $L^{(\ell)}(\theta)$ controls the W^ℓ -distance between the trained network’s restriction $\Pi_{\Gamma^\ell}[\rho_\theta]$ and the discrete solution $\rho_{N_\ell}^*$. The estimate (7) bounds the further gap from $\rho_{N_\ell}^*$ to $\Pi_{\Gamma^\ell}[\rho^*]$ by $\mathcal{O}(h_\ell^\nu)$, so driving $L^{(\ell)}$ much below $\mathcal{O}(h_\ell^{2\nu})$ does not improve the trained network’s accuracy against the continuum solution at level ℓ . A practical choice is therefore $\varepsilon_t \propto h_{s_t}^{2\nu}$, the per-stage tolerance set from the resolution of the grid Γ^{s_t} visited at stage t ; under a cyclic schedule a level revisited later in the schedule is assigned a tighter tolerance than on its earlier visit, as in the per-stage targets of Table 5. (Section 3.5 adds a complementary $\mathcal{O}(h_\ell^{2q})$ floor from the network’s C^q -regularity in Assumption 3.1; the two coincide when $q \geq \nu$, which holds automatically for smooth-activation networks.) The remaining hyperparameters (learning-rate schedules and batch size) can be tuned at the coarsest level, where each Adam step is inexpensive, and held fixed across all stages.

Two scenarios at near-stationarity. Write θ for the current parameter, and suppose the level- ℓ optimization has run long enough that

$$\nabla_\theta L^{(\ell)}(\theta) = (J_\theta^{(\ell)})^* A_{N_\ell}^* r_\theta^{(\ell)} \approx 0. \quad (47)$$

A small gradient in \mathbb{R}^p admits two distinct explanations. **(S1)** The residual is itself small, $r_\theta^{(\ell)} \approx 0$, so θ is near a level- ℓ minimizer in the sense of (43). **(S2)** The residual is not small, but $A_{N_\ell}^* r_\theta^{(\ell)}$ lies in $\ker(T_\theta^{(\ell)})$, the W^ℓ -orthogonal complement of the column space of $J_\theta^{(\ell)}$: the parameter-space gradient cannot see it, and the optimizer is trapped at a suboptimal stationary point of $L^{(\ell)}$ where the empirical NTK has lost rank along the residual direction. Our experiments at the coarser levels are consistent with (S1). Refinement revives the gradient under either scenario, since every factor is rebuilt on the finer grid; the resulting warm-start bound is developed in Section 3.5.

3.5 Cross-level residual transfer

We now examine what the optimizer hands off between successive levels. After level- ℓ training to tolerance ε_ℓ , the parameter $\theta^{(\ell, \text{end})}$ is passed to level $\ell + 1$ as the warm start, and the level- $\ell + 1$ residual $r_{\theta^{(\ell, \text{end})}}^{(\ell+1)}$ becomes the initial condition for the level- $\ell + 1$ optimizer. The argument below works through the continuum residual $r_\theta := \mathcal{A}\rho_\theta - g$ on Γ , of which $r_\theta^{(\ell)}$ and $r_\theta^{(\ell+1)}$ are discrete samples; it is independent of any specific relationship between the grids and does not require, in particular, that they be nested.

The level- $\ell + 1$ loss $L^{(\ell+1)}(\theta^{(\ell, \text{end})})$ receives two qualitatively different contributions, corresponding to two distinct things training at level ℓ does and does not control.

(I) Inherited from level- ℓ training. Training at level ℓ to tolerance ε_ℓ pins the residual small at the Γ^ℓ nodes: $\|r_\theta^{(\ell)}\|_{W^\ell}^2 \leq 2\varepsilon_\ell$. The values of r_θ on Γ^ℓ control, via quadrature consistency, a corresponding part of $\|r_\theta\|_{L^2(\Gamma)}^2$, and this part enters $L^{(\ell+1)}$.

(II) The off-grid residual. The values of r_θ off Γ^ℓ are not constrained by level- ℓ training; they are the off-grid, high-frequency content that grid refinement re-exposes (Section 3.3).

The level- $\ell + 1$ optimizer must drive both contributions to the target tolerance. Contribution (I) is amortized to the level- ℓ tolerance from the start; (II) requires fresh work and dominates.

Total work under a regularity hypothesis on the network. In a mesh-based multilevel method the object carried between levels is a grid function, and the prolongation error it incurs is controlled by interpolation estimates that invoke the regularity of the underlying solution. Here the object carried between levels is the network itself, a single globally parameterized function on Γ evaluated on grids of different resolutions, and the cross-level error is the off-grid residual identified above. The counterpart of the interpolation esti-

mate is therefore a regularity bound on the represented function, and we postulate one that holds uniformly throughout training.

Assumption 3.1. *There exist an integer $q \geq 1$ and a constant $C_\rho < \infty$ such that, for every parameter θ encountered during training, $\rho_\theta : \Gamma \rightarrow \mathbb{R}$ belongs to $C^q(\Gamma)$ with $\|\rho_\theta\|_{C^q(\Gamma)} \leq C_\rho$, where $\|\rho\|_{C^q(\Gamma)} := \max_{0 \leq j \leq q} \sup_{x \in \Gamma} |\nabla_\Gamma^j \rho(x)|$ is the largest sup-norm over Γ of the surface derivatives of ρ up to order q (∇_Γ the tangential gradient on Γ).*

Under Assumption 3.1, and provided $g \in C^q(\Gamma)$ and the kernel k is smooth enough that \mathcal{K} maps $C^q(\Gamma)$ into itself, the continuum residual $r_\theta = \frac{1}{2}\rho_\theta + \mathcal{K}\rho_\theta - g$ is also C^q on Γ with C^q -norm bounded uniformly by a constant depending only on C_ρ , the kernel k , and the boundary data g . Sampling estimates for C^q functions on the quasi-uniform node set Γ^ℓ of fill distance h_ℓ , combined with quadrature consistency, give

$$\|r_\theta\|_{L^2(\Gamma)}^2 \leq C \underbrace{\|r_\theta^{(\ell)}\|_{W^\ell}^2}_{\text{(I) inherited}} + C \underbrace{h_\ell^{2q}}_{\text{(II) off-grid residual}}, \quad (48)$$

The underlying sampling inequality bounds $\|r_\theta\|_{L^2(\Gamma)}^2$ by the values of r_θ on Γ^ℓ plus a remainder $\mathcal{O}(h_\ell^{2q} \|r_\theta\|_{C^q(\Gamma)}^2)$ set by the fill distance; the weighted node values are the discrete residual $\|r_\theta^{(\ell)}\|_{W^\ell}^2$, contribution (I), and the uniformly bounded C^q -norm makes the remainder the $\mathcal{O}(h_\ell^{2q})$ off-grid contribution (II). Combining with the level- ℓ training tolerance $\|r_\theta^{(\ell)}\|_{W^\ell}^2 \leq 2\varepsilon_\ell$ gives

$$\|r_\theta\|_{L^2(\Gamma)}^2 \leq C (\varepsilon_\ell + h_\ell^{2q}). \quad (49)$$

The level- $\ell + 1$ loss $L^{(\ell+1)}(\theta) = \frac{1}{2}\|r_\theta^{(\ell+1)}\|_{W^{\ell+1}}^2$ is the quadrature image of $\frac{1}{2}|r_\theta|^2$ on $\Gamma^{\ell+1}$, hence bounded by a constant times $\|r_\theta\|_{L^2(\Gamma)}^2$, giving the warm-start loss bound

$$L^{(\ell+1)}(\theta^{(\ell, \text{end})}) \leq C (\varepsilon_\ell + h_\ell^{2q}), \quad (50)$$

with C depending only on C_ρ , k , g , and $|\Gamma|$. The Lipschitz case $q = 1$ gives $L^{(\ell+1)} \leq C(\varepsilon_\ell + h_\ell^2)$; higher regularity of the network output sharpens the bound proportionally.

The same split shapes the spectral content of the correction, not just its size. The off-grid term h_ℓ^{2q} is fixed by the grid, while the inherited term ε_ℓ falls with the level- ℓ tolerance, so tightening ε_ℓ raises the share of the warm-start loss carried by the off-grid modes, the newly exposed higher modes onto which level $\ell + 1$ must expand \mathcal{E}_θ . Converging each level well thus concentrates the next level's fresh work on its own band, the spectral counterpart of multigrid's band-by-band clearing. The gain saturates at the matched tolerance $\varepsilon_\ell \propto h_\ell^{2q}$: pushed below it, the inherited residual is driven beneath the accuracy the finer grid can use, fitting the coarse grid's quadrature error rather than the solution.

With the matched tolerance schedule $\varepsilon_\ell \propto h_\ell^{2q}$, (50) gives $L^{(\ell+1)}(\theta^{(\ell, \text{end})}) = \mathcal{O}(h_\ell^{2q}) = \mathcal{O}(\varepsilon_{\ell+1})$: the level- $\ell + 1$ optimizer starts within a constant factor of its target tolerance, and a number of MINIRES iterations bounded independently of ℓ , set only by the per-iteration contraction rate of Section 3.2, suffices to drive $L^{(\ell+1)}$ to $\varepsilon_{\ell+1}$. With per-iteration arithmetic $\mathcal{O}(b N_\ell)$, the total work across L levels is bounded by

$$W_{\text{total}} \leq C \sum_{\ell=1}^L b N_\ell = \mathcal{O}(b N_L), \quad (51)$$

a constant multiple of the work at the finest grid alone.

The estimates (48)–(51) use each grid only through its own fill distance, quasi-uniformity constants, and positive weights; no relation between Γ^ℓ and $\Gamma^{\ell+1}$ enters, since every step passes through the continuum

residual r_θ . Nested ladders and ladders whose node sets are pairwise disjoint are therefore covered on the same footing. What the argument does require is global coverage at every level: each Γ^ℓ must sample all of Γ quasi-uniformly, with constants bounded uniformly in ℓ , since a grid that leaves a region of Γ unsampled defeats the sampling estimate behind (48) there.

For a C^q activation function on \mathbb{R} , composition gives $\rho_\theta \in C^q(\Gamma)$ for every $\theta \in \mathbb{R}^p$, with C^q -norm finite at any fixed θ . Whether that norm stays bounded throughout training is the non-trivial part. In overparameterized networks, the level sets of $L^{(\ell)}(\theta)$ are manifolds of positive dimension, and the gradient flow (19) can drift along such a manifold with the loss essentially constant but $\|\theta\|$ growing. Convergence of the per-level loss therefore does not imply convergence or even boundedness of θ , and Assumption 3.1 can fail across the stages even when every per-level training has converged in loss. An ℓ^s weight-decay term $\lambda \|\theta\|_s^s$ (e.g., $s = 2$) in the per-level loss makes it coercive in θ and pins the trajectory in a bounded region of \mathbb{R}^p , enforcing Assumption 3.1. Section 4 gives a numerical illustration of the effect on the off-grid residual.

4 Numerical examples

We solve two model problems: an interior Dirichlet problem for Poisson’s equation and an exterior Neumann problem for the Helmholtz equation. These problems involve both real- and complex-valued density functions, with the corresponding boundary integrals represented using either parametric or volumetric surface descriptions. The discrete operators are well-conditioned in both cases, so the analysis of Section 3 applies as written.

Problem 1: Interior Dirichlet for Poisson. On a bounded domain $\Omega \subset \mathbb{R}^d$, $d \in \{2, 3\}$, with C^2 boundary $\Gamma = \partial\Omega$, find u satisfying

$$\Delta u = f \quad \text{in } \Omega, \quad u = g \quad \text{on } \Gamma.$$

Writing $u = u_p + v$ with u_p a known particular solution of $\Delta u_p = f$, the harmonic correction v inherits Dirichlet trace $g - u_p|_\Gamma$. We represent v as a double-layer potential

$$v(x) = \int_\Gamma \frac{\partial G_0(x, y)}{\partial n_y} \rho(y) dS(y), \quad x \in \Omega, \tag{52}$$

with G_0 the Laplace fundamental solution

$$G_0(x, y) = \begin{cases} -\frac{1}{2\pi} \log |x - y|, & d = 2, \\ \frac{1}{4\pi} |x - y|^{-1}, & d = 3. \end{cases}$$

The interior-Dirichlet jump relation [14] then yields the second-kind BIE (1) for ρ with right-hand side $g - u_p|_\Gamma$ and double-layer kernel

$$k_{\text{Lap}}(x, y) = \frac{\partial G_0(x, y)}{\partial n_y}. \tag{53}$$

The pure Laplace case is recovered for $f \equiv 0$, in which case $u_p \equiv 0$ and the BIE right-hand side reduces to g .

Problem 2: Exterior Neumann for Helmholtz. On the exterior $\mathbb{R}^3 \setminus \bar{\Omega}$, find u satisfying

$$\Delta u + \kappa^2 u = 0 \quad \text{in } \mathbb{R}^3 \setminus \bar{\Omega}, \quad \frac{\partial u}{\partial n} = g \quad \text{on } \Gamma,$$

together with the Sommerfeld radiation condition at infinity. We seek u as a single-layer potential

$$u(x) = \int_{\Gamma} G_{\kappa}(x, y) \rho(y) dS(y), \quad x \in \mathbb{R}^3 \setminus \bar{\Omega}, \quad (54)$$

with the radiating Helmholtz Green's function

$$G_{\kappa}(x, y) = \frac{e^{i\kappa|x-y|}}{4\pi|x-y|}.$$

Taking the normal derivative on the exterior side and applying the jump relation gives the second-kind BIE (1) with right-hand side proportional to g and kernel

$$k_{\text{Helm}}(x, y) = \frac{\partial G_{\kappa}(x, y)}{\partial n_x}. \quad (55)$$

The sign of the jump is opposite to that in (1), which the convention there absorbs.

Caveat: spurious resonance. The single-layer formulation (54)–(55) of the exterior Neumann Helmholtz problem loses unique solvability at wavenumbers κ for which κ^2 is an interior Dirichlet eigenvalue of $-\Delta$ on Ω , and is ill-conditioned for κ near such a resonance. The combined-field formulation of Burton and Miller [5] restores uniqueness; we do not pursue that extension here. Our purpose is to demonstrate the MLSG as a computational algorithm, and we choose test wavenumbers away from the interior Dirichlet spectrum of Ω .

Surface representations and the network. We test each problem under two representations of the density ρ . The discretization details for both are deferred to Appendix A; here we record only what the reader needs to interpret the experiments and, in particular, what the quadrature node set Γ_N looks like in each case.

Parametric representation $\rho_{\theta}^{\text{param}}$. When Γ admits a finite atlas $\{(D_{\alpha}, \varphi_{\alpha})\}_{\alpha=1}^{M_{\text{chart}}}$ with charts $\varphi_{\alpha} : D_{\alpha} \subset \mathbb{R}^{d-1} \rightarrow \Gamma_{\alpha} \subset \Gamma$ and $\Gamma = \bigcup_{\alpha} \Gamma_{\alpha}$, we use one MLP per chart and write the full collection as a vector indexed by the charts,

$$\rho_{\theta}^{\text{param}} = (\rho_{\theta(1)}, \dots, \rho_{\theta(M_{\text{chart}})}), \quad \rho_{\theta(\alpha)} : D_{\alpha} \rightarrow \mathbb{C}, \quad \alpha = 1, \dots, M_{\text{chart}},$$

with parameter blocks $\theta = (\theta(1), \dots, \theta(M_{\text{chart}}))$ and $\theta(\alpha) \in \mathbb{R}^{p_{\alpha}}$ the parameters of the chart- α network. The chart index α is written in parentheses to keep it visually separate from the per-component subscript θ_k of Section 2.3. The surface density is defined by composition through the appropriate chart,

$$\rho(\varphi_{\alpha}(\xi)) = \rho_{\theta(\alpha)}(\xi), \quad \xi \in D_{\alpha},$$

and the BIE data pulls back as $g_{\alpha} := g \circ \varphi_{\alpha}$. Each quadrature node $x_j \in \Gamma_N$ is the image $x_j = \varphi_{\alpha}(\xi_j^{\alpha})$ of a node ξ_j^{α} on some chart α , and the resulting operator A_N is block $M_{\text{chart}} \times M_{\text{chart}}$ in the chart partition; the diagonal blocks contain the on-chart singular interactions and use a singularity-aware quadrature, while the off-diagonal blocks evaluate the kernel between distinct chart images and are smooth. The solver of Section 3 acts on the concatenated parameters θ , with the per-level loss summed over charts. The atlas-level integral split, the explicit discrete equations, and the two-chart block linear system are written out in Appendix A.1.

Volumetric (IBIM) representation $\rho_{\theta}^{\text{IBIM}}$. When Γ is given non-parametrically as the zero level set of a signed distance function d_{Γ} , we adopt the implicit boundary integral method (IBIM) of [15, 6], with a single ambient MLP

$$\rho_{\theta}^{\text{IBIM}} : \mathbb{R}^d \rightarrow \mathbb{C},$$

whose trace on Γ is optimized by the solver. The quadrature nodes $x_j \in \Gamma_N$ are the closest-point projections $x_j = P_\Gamma(z_j)$ of nodes z_j of a Cartesian grid that fall in a thin tubular neighborhood $T_\epsilon = \{x \in \mathbb{R}^d : |d_\Gamma(x)| < \epsilon\}$, with weights absorbing a regularized one-dimensional delta in d_Γ . The full tubular rule and the IBIM-discretized K_N are written out in Appendix A.2.

Neural network architecture. Across all experiments, the density is represented by a multilayer perceptron with sinusoidal activations and the SIREN initialization [18], which draws the input-layer weights from $\mathcal{U}[-\omega_0 d, \omega_0 d]$ and the hidden-layer weights from $\mathcal{U}[-\sqrt{6}/n, \sqrt{6}/n]$, with n the layer width. The depth, the width, and the frequency parameter ω_0 vary across problems and are recorded in the corresponding subsections. Unless stated otherwise, the network is trained with the Adam optimizer from an initial learning rate of 10^{-3} , decayed by a factor of 0.9 every 200 epochs, with mini-batches of 8192 rows and a weight decay of 10^{-6} .

Practical loss implementation. The solver minimizes the *unweighted* (Euclidean) residual $\frac{1}{2} \sum_i |r_\theta(x_i)|^2$, the discrete loss (11) with W replaced by the identity, while A_N is assembled with the quadrature weights throughout. This leaves the target unchanged: the discrete system is consistent, so both losses vanish at the same $\rho_N^* = A_N^{-1} g_N$. The spectral-bias and tangent-space phenomena of Sections 3.2–3.3 concern the spectrum of the empirical NTK and hold in the Euclidean inner product just as in the W -weighted one, so they are unaffected by the choice $W = I$. The residual-norm equivalence on a quasi-uniform quadrature,

$$\min_j w_j \|v\|_2^2 \leq \|v\|_W^2 \leq \max_j w_j \|v\|_2^2, \quad \kappa_W := \sqrt{\max_j w_j / \min_j w_j}, \quad (56)$$

governs instead the quantitative side: the a posteriori error bound (Lemma 2.1) and the cross-level constants (Section 3.5) carry over with κ_W in place of their weighted values. For the IBIM discretization $W = I$ is moreover the *natural* choice, consistent with the surface geometry: the unweighted loss is the tube-volume average of the residual and approximates the surface L^2 loss with the same minimizer (Proposition A.1). The chart-based discretizations (Appendix A.1) carry a κ_W above 1, though weighting matters only for severely non-uniform discretizations such as corners or graded meshes. We use $W = I$ deliberately: it is the unbiased mini-batch estimator of the residual under uniform node sampling, it is the plain mean-squared residual minimized by other neural solvers, so the reported speedups isolate the multilevel schedule rather than a bespoke weighting.

Computational facilities. All neural networks are implemented and trained in PyTorch on a single Nvidia H200 GPU, provided by the National Center for High-Performance Computing (NCHC), National Institutes of Applied Research (NIAR), Taiwan. For comparison, reference solutions are computed using `gmres()` in MATLAB 2024B on the NCHC Forerunner 1 computer with 64 Intel Xeon Platinum 8480+ CPUs and 275.2GB RAM. In addition, `gmres()` accepts a restart parameter m that caps the Krylov subspace dimension, bounding memory and orthogonalization cost at the expense of slower convergence. We set $m = 60$ in all experiments.

4.1 The spectral bias and expansion of effective neural tangent spaces

This subsection reports experiments supporting the spectral analysis of Sections 3.2 and 3.3: at a trained parameter θ , the empirical NTK $T_{\theta,N}$ has a small leading band of eigenvalues that confines the effective neural tangent space \mathcal{E}_θ to a few modes; refining the grid extends \mathcal{E}_θ to higher modes; and the residual at each warm start concentrates outside the previous level’s \mathcal{E}_θ and inside the new one.

We consider the Laplace equation on a two-dimensional flower-shaped domain whose boundary Γ is parametrized by

$$x(s) = A(s) \cos s, y(s) = A(s) \sin s, A(s) = \frac{\sqrt{5}}{50} + (1 + 0.1 \sin(4s)), \quad s \in [0, 2\pi). \quad (57)$$

with Dirichlet data

$$g(x(s), y(s)) = y(s)(1 - \sin(150s)), \quad s \in [0, 2\pi). \quad (58)$$

The density ρ is represented by a single MLP that takes the Cartesian coordinates $(x(s), y(s))$ as input, with 8 hidden layers of 200 neurons each and \cos activations. We adopt Kaiming initialization here.

The experiment uses the grid ladder has $L = 5$ levels with $N_\ell = 2^{6+\ell}$ quadrature points for $\ell = 1, \dots, 5$, so the coarsest grid carries 128 points and the finest carries 2048. At each level, $\kappa_W \approx 1.2306$. The early-stopping tolerance is $\varepsilon_1 = 1.6 \times 10^{-4}$ at the coarsest level and is halved at each refinement, reaching $\varepsilon_5 = 10^{-5}$ at the finest. Under this schedule the solver reliably drives the training residual below 10^{-5} on the finest grid. In contrast, *the single-level runs on the same finest grid does not reach this threshold after 20,000 iterations*. See Figure 3.

Spectral expansion across levels. Figures 1 and 2 report the NTK spectra at the start and at termination of Levels 1–4, aggregated over 20 independent runs. The top row of each figure shows the spectrum of T_{θ, N_ℓ} (the level- ℓ empirical NTK $T_\theta^{(\ell)}$ of Section 3.4); the bottom row shows the residual projected onto its eigenmodes. Two trends are visible. First, the leading band of T_{θ, N_ℓ} widens with ℓ : the effective dimension of \mathcal{E}_θ inherited at the start of each new level is larger than at the start of the previous level. Second, the residual entering each level concentrates in modes that have just become reachable, so the gradient flow on that level acts directly on it. This is the cross-level mechanism analyzed in Section 3.5.

Progressive versus cyclic schedules. Figure 4 compares the two visiting schedules of Section 3.4 on this example over 50 independent runs. The effective neural tangent spaces at the end of training are comparable under the two schedules, and so are the mean computation times. The difference lies in the spread: the networks trained under the cyclic schedule show markedly smaller variance, both in the number of gradient updates and in the wall-clock time.

4.2 Poisson’s equation in three dimensions

We apply the MLSG to a Poisson problem on the Stanford bunny, a non-convex three-dimensional surface with regions of relatively high curvature. The surface is given non-parametrically through a signed distance function, and the density is represented volumetrically via the IBIM scheme of Appendix A.2. The example demonstrates that the MLSG remains effective on geometries that do not admit a convenient atlas and that demand local refinement to resolve high-curvature features — a requirement that any consistent quadrature scheme inherits, since the continuous second-kind operator on Γ is well-conditioned only to the extent that the geometry is resolved by the discretization.

We use IBIM to solve

$$\Delta u = 1 \quad \text{in } \Omega, \quad u = \frac{1}{6}(x^2 + y^2 + z^2) \quad \text{on } \partial\Omega, \quad (59)$$

whose exact solution is the boundary datum extended into Ω , so the relative L^2 error in the reconstructed u admits a closed-form reference.

The geometry $\partial\Omega$ is given as a dense point cloud sampled from the Stanford bunny. On grid nodes surrounding the point cloud, local piecewise quadratic interpolation is used to evaluate the distance values and

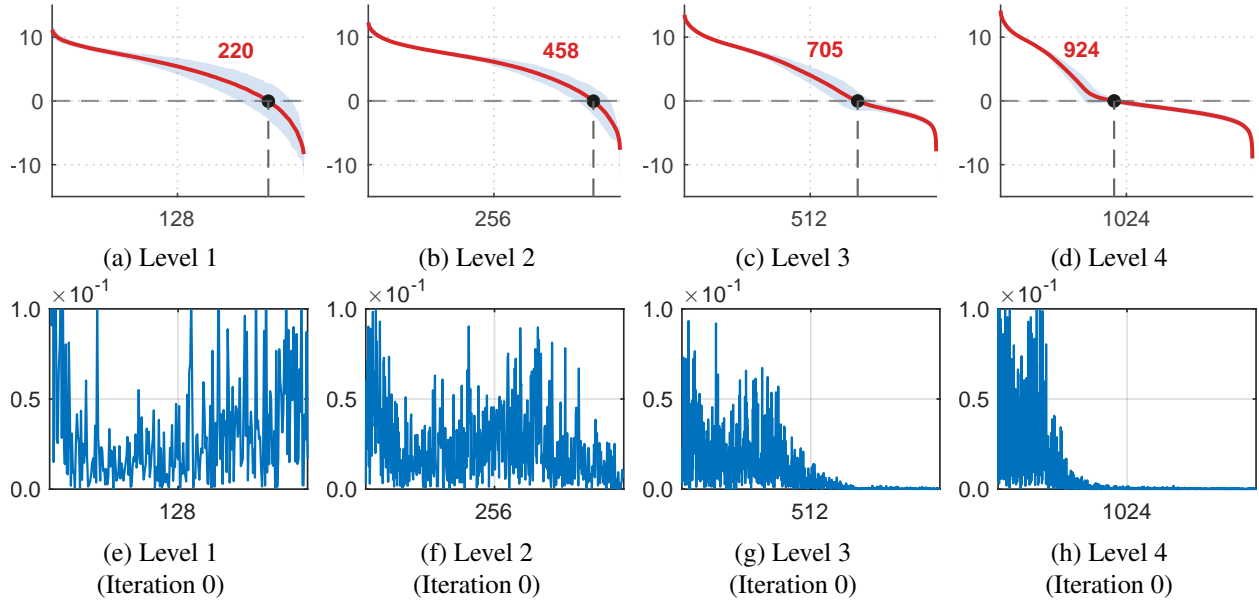


Figure 1: Initial NTK spectral distributions at Levels 1–4, aggregated over 20 independent runs. Top: NTK spectra. Bottom: errors projected on NTK’s eigenmodes.

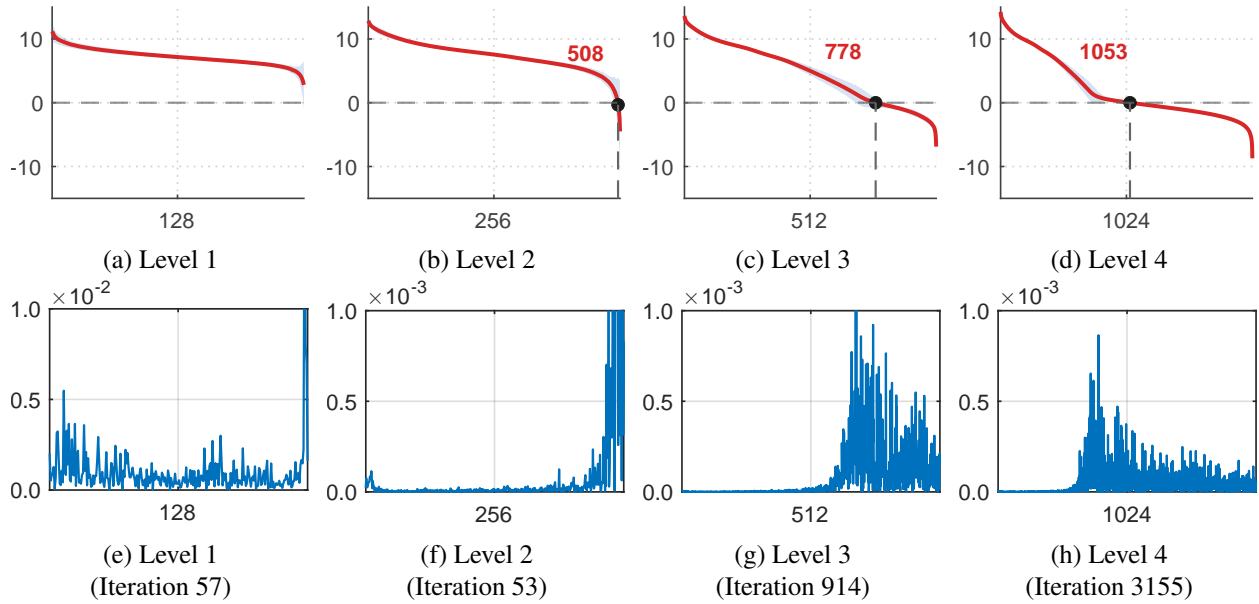


Figure 2: NTK spectral distributions upon termination at Levels 1–4, aggregated over 20 independent runs, under the same setup and layout as the initial state shown in Fig. 1. Comparing the two reveals how the spectra and projected errors evolve from initialization (Iteration 0) to convergence (Iterations 57, 53, 914, and 3155 for Levels 1–4, respectively). Top: NTK spectra. Bottom: errors projected on NTK’s eigenmodes.

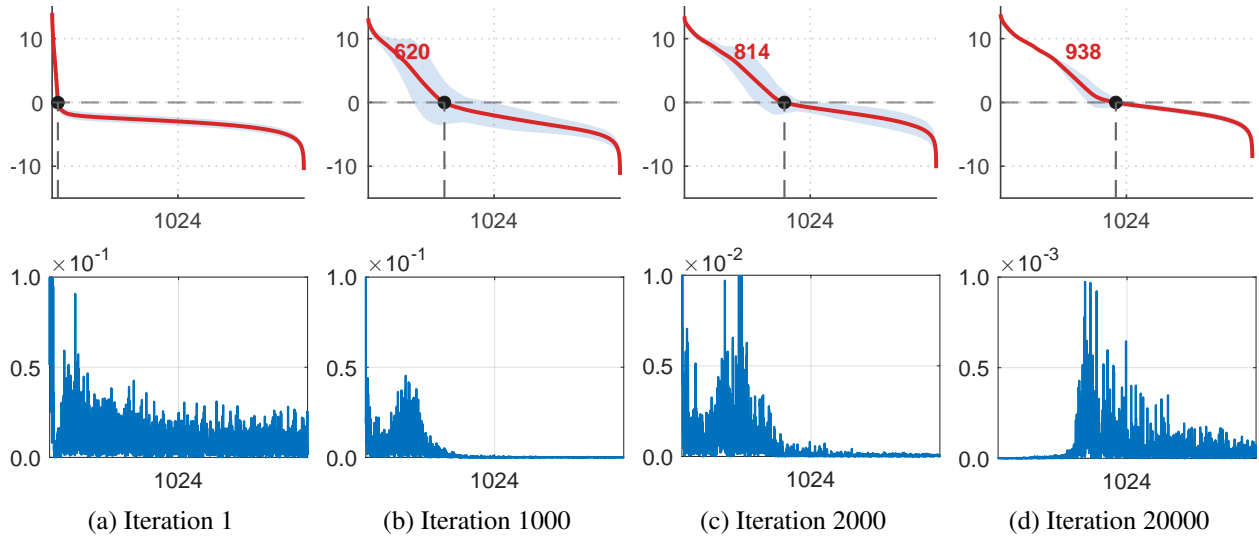


Figure 3: Single-level training on the finest grid: NTK spectra at iterations 1, 1000, 2000, and the final step. Top: NTK spectra. Bottom: errors projected on NTK’s eigenmodes. Loss at iteration 20,000 is 2.21×10^{-5} .

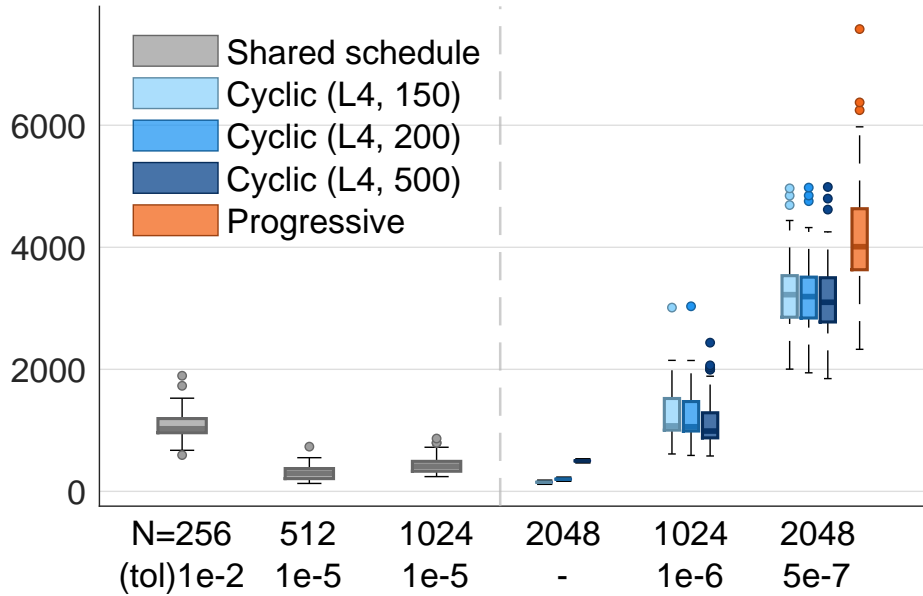


Figure 4: Box plots of epoch counts at each training level comparing the progressive and cyclic schedules over 50 independent runs. The first three levels ($N = 256, 512, 1024$) are shared between both methods (gray). For the cyclic schedule, levels 5 and 6 report the iteration counts after different prescribed epoch budgets at level 4 (150, 200, 500 epochs; light to dark blue). For the progressive schedule, the final level reports the iterations needed to reach the prescribed tolerance.

the Jacobian needed in the IBIM formulation. In this experiment, we use a 10 layers with 500 hidden nodes per layer fully connected neural network, in which we use sin and the SIREN for as our activation function and initialization respectively.

Table 1 records the training progression.

Table 1: MLSG (progressive) training statistics for the Stanford bunny example. The epoch and time columns report the mean and standard deviation over 20 Monte Carlo trials in separate sub-columns. The Total row reports the mean and standard deviation of the per-trial totals.

Level	Grid	Problem size	Target loss	Epochs		Time (s)	
				Mean	Std	Mean	Std
0	40^3	10 000	8.0×10^{-4}	45.75	4.74	1.10	0.34
1	64^3	26 082	4.0×10^{-4}	32.15	3.00	3.35	0.34
2	81^3	41 974	2.0×10^{-4}	20.95	1.28	4.96	0.31
3	102^3	66 664	2.0×10^{-4}	19.25	0.91	10.68	0.51
4	128^3	104 663	1.5×10^{-4}	15.45	0.83	19.89	1.07
5	161^3	164 198	1.5×10^{-4}	15.55	0.60	48.73	1.90
6	203^3	256 242	1.5×10^{-4}	8.90	0.45	66.26	3.32
7	256^3	394 457	1.5×10^{-4}	8.15	0.49	142.00	8.54
Total						296.96	11.70

We compare the neural-network solution with the solution obtained by GMRES. Both methods are evaluated using the squared relative L^2 error, with a target accuracy of 10^{-3} . Figure 5 reports the surface density and the pointwise errors evaluated at sampled interior points.

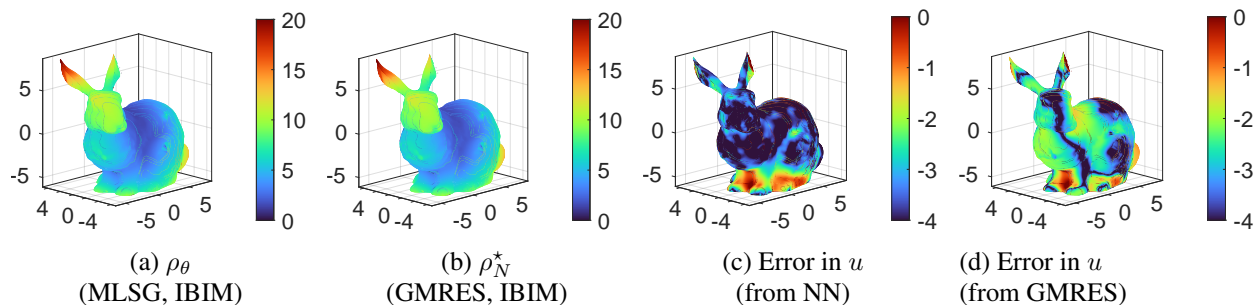


Figure 5: Stanford Bunny example. The first two panels show the surface density obtained by the neural-network solver and by GMRES, respectively. The last two panels show the corresponding pointwise errors evaluated at sampled interior points.

4.3 Exterior Helmholtz problem in three dimensions

We test the MLSG on the exterior Neumann problem for the Helmholtz operator at moderate-to-high wavenumber. Two groups of experiments are reported. The first is a wall-clock and accuracy benchmark on a canonical multi-sphere scatterer. The second is a stress test on geometries that admit no convenient single chart or whose topology is non-trivial, demonstrating that the MLSG remains effective on shapes that fall outside the standard parametric setting.

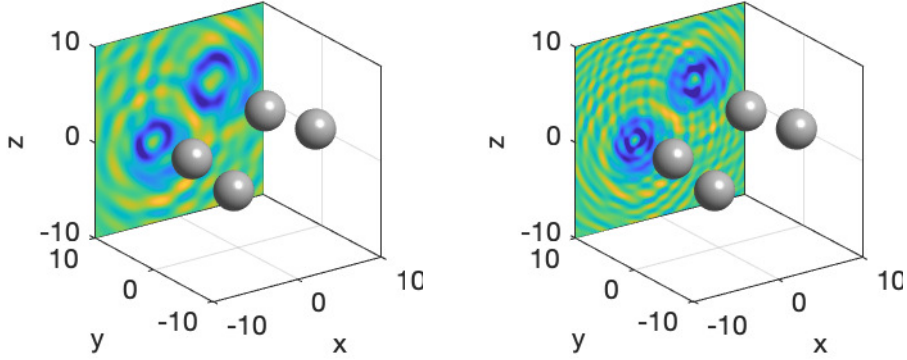


Figure 6: Total wave field $|u + u^{inc}|$ reconstructed from the MLSG density. (left) $n = 256$ points per dimension, $\kappa = 4$. (right) $n = 512$ points per dimension, $\kappa = 8$.

4.3.1 Scattering by multiple spheres

The multi-sphere configuration is the canonical three-dimensional Helmholtz benchmark and the natural setting for our wall-clock comparison with GMRES. We report two experiments: how the MLSG runtime scales with the number of obstacles at fixed grid resolution, and how it scales with the grid resolution and the wavenumber on the four-sphere configuration. Throughout this subsection we write n for the per-dimension Cartesian grid resolution, to keep N reserved for the total quadrature point count on Γ as elsewhere in the paper.

Each scatterer is a radius-2 ball placed inside the cubic computational box $[-10, 10]^3$; configurations are arranged so that the shortest center-to-center distance between spheres is 2.7. The incident field is the plane wave $u^{inc} = \exp(i\kappa y)$, with a chosen wave number κ ; the Neumann data on $\bigcup_j \partial B_j$ is the negative of its normal derivative, and (54)–(55) apply on each sphere with off-diagonal blocks of K_N carrying the inter-sphere coupling. All test wavenumbers κ are chosen away from the interior Dirichlet spectrum of $\bigcup_j B_j$.

The network has 5 hidden layers of 200 neurons with SIREN activations ($\omega_0 = 1$); mini-batches contain 1024 rows. The grid ladder has $L = 4$ levels with per-dimension grid resolution increasing by $\sqrt{2}$ at each step, so the total quadrature point count doubles across levels. The learning rate is 10^{-3} for the first two levels and 10^{-4} for the remaining two.

Scaling with the number of obstacles. Holding the per-dimension grid at $n = 256$ and the wavenumber at $\kappa \in \{1, 4\}$, we progressively add radius-2 balls (one through seven) to the box and record the MLSG wall-clock time. Table 2 reports the resulting timings. The runtime grows with the number of scatterers and is generally larger at $\kappa = 4$ than at $\kappa = 1$, reflecting the denser angular content the network must represent at higher wavenumbers.

Table 2: MLSG (progressive) mean wall-clock time (in seconds) at $n = 256$ as the number of randomly placed, non-overlapping, radius-2 balls increases, for wavenumbers $\kappa = 1$ and $\kappa = 4$. The shortest center-to-center distance between spheres equal to 2.7.

Balls	1	2	3	4	5	6	7
$\kappa = 1$	8.80	26.10	38.49	30.69	62.73	89.70	146.21
$\kappa = 4$	15.49	29.92	35.98	62.08	88.59	145.83	228.99

Table 3: Wall-clock comparison for the four-sphere Helmholtz benchmark, GMRES against the MLSG under the progressive schedule at matched accuracy. The MLSG mean and standard deviation are over 20 trials, reported in separate sub-columns.

Grid spacing h	Problem size	κ	GMRES (s)	MLSG (s)		Speedup
				Mean	Std	
0.078	131 030	1	3 194.60	35.13	4.51	90.93
		2	5 126.90	26.69	1.94	192.09
		3	9 871.70	36.22	4.33	272.55
		4	12 080.78	65.40	10.53	184.72
0.039	525 182	1	18 949.67	199.75	4.21	94.87
		3	70 434.94	128.81	18.85	546.81
		5	56 394.54	140.61	21.26	401.07
		7	259 602.63	4,310.79	1,187.89	60.22
		8	–	1,598.65	369.67	–

Scaling with grid resolution and wavenumber. On the four-sphere configuration we vary the per-dimension grid resolution $n \in \{256, 512\}$ (problem sizes 131, 030 to 525 182 quadrature nodes on Γ) and the wavenumber κ across the values listed in Table 3.

The table compares the MLSG wall-clock time against multi-core MATLAB GMRES at matched accuracy. The wavenumber κ enters the condition number of the Helmholtz BIE operator, so the GMRES iteration count, and with it the wall-clock time, generally grows with κ (Table 3); on the largest grid at $\kappa = 8$ the run was terminated at the cluster’s four-day wall-time limit.

Figure 6 shows two-dimensional slices of the total wave field reconstructed from the MLSG density.

The MLSG output can also serve as the initial guess for a conventional iterative solver when accuracy beyond the MLSG tolerance is required.

4.3.2 Scattering by nonconvex surfaces

Coiled torus. We solve the Helmholtz equation exterior to a coiled torus, a tube of circular cross-section whose centerline winds twelve times around a large circle, giving a strongly nonconvex surface. With $(t, s) \in [0, 2\pi]^2$ the surface is

$$\mathbf{X}(t, s) = \mathbf{c}(t) + r_{\text{tube}}(\cos s \mathbf{N}(t) + \sin s \mathbf{B}(t)), \quad (60)$$

with centerline

$$\mathbf{c}(t) = ((5 + 0.9 \cos 12t) \cos t, (5 + 0.9 \cos 12t) \sin t, 0.9 \sin 12t),$$

tube radius $r_{\text{tube}} = 0.5$, and

$$\mathbf{N}(t) = (\cos 12t \cos t, \cos 12t \sin t, \sin 12t), \quad \mathbf{B}(t) = \hat{\mathbf{T}}(t) \times \mathbf{N}(t), \quad \hat{\mathbf{T}}(t) = \mathbf{c}'(t)/|\mathbf{c}'(t)|,$$

the normal and binormal along the centerline. The surface is rotated so that the axis of the large circle points along $(3, 4, 5)/\sqrt{50}$, tilting it out of the coordinate planes. The incident field is the plane wave

$u^{inc} = \exp(i\kappa y)$, with a chosen wavenumber κ . A single doubly periodic chart covers the surface, so the parametric representation applies with one network module $\rho_\theta^{\text{param}}$; the interval $[0, 2\pi]$ is partitioned into N subintervals in each angular variable, giving a system matrix $A_N \in \mathbb{C}^{N^2 \times N^2}$. The network has 10 hidden layers of 500 neurons with SIREN activations.

Figure 7 shows the computed density and the recovered total field at $\kappa = 8$ with $N = 1024$ (system size $N^2 = 1,048,576$); the MLSG solve took 4,621.6 s of wall-clock time.

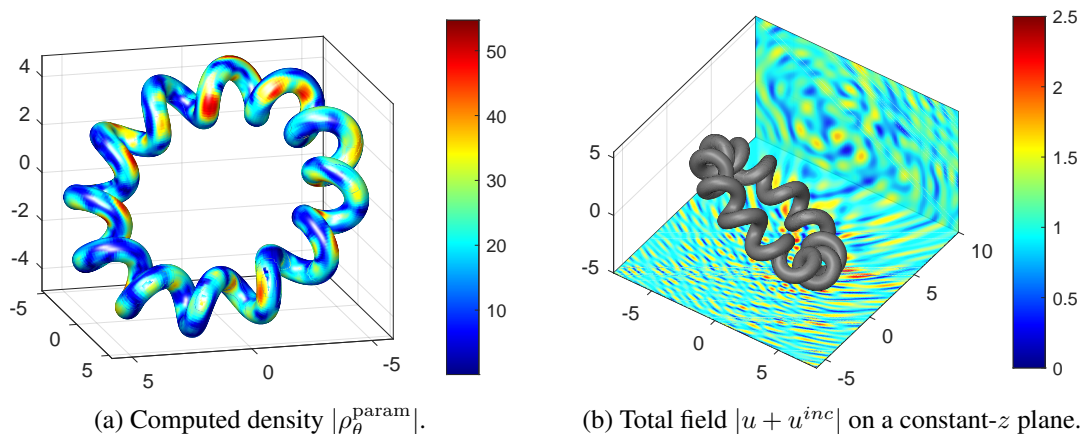


Figure 7: Coiled-torus Helmholtz problem ($\kappa = 8$, $N = 1024$, system size $N^2 = 1,048,576$) with a zero Neumann boundary condition and an incident plane wave $u^{inc} = \exp(i\kappa y)$.

Linked tori. We now turn to a more intricate configuration: two congruent tori linked into a chain. With major radius $R = 4$ and minor radius $r = 1$, the tori are parametrized by

$$\begin{aligned} \mathbf{X}_1(t, s) &= ((R + r \cos s) \cos t, r \sin s, (R + r \cos s) \sin t), \\ \mathbf{X}_2(t, s) &= ((R + r \cos s) \cos t + R, (R + r \cos s) \sin t, r \sin s), \quad 0 \leq t, s < 2\pi, \end{aligned}$$

and the configuration is contained in the box $[-20, 20]^3$. The incident field is the plane wave $u^{inc} = \exp(i\kappa y)$, with a chosen wave number κ . Each torus is covered by a single doubly periodic chart, so the parametric representation applies with one network module per torus, $\rho_\theta^{\text{param}} = (\rho_{\theta(1)}, \rho_{\theta(2)})$. The interval $[0, 2\pi]$ is partitioned into N subintervals in each angular variable to generate the grid points on each torus.

Discretizing the BIE yields a linear system in block form,

$$\begin{bmatrix} A_{11} & A_{12} \\ A_{21} & A_{22} \end{bmatrix} \begin{bmatrix} \rho_{1,N} \\ \rho_{2,N} \end{bmatrix} = \begin{bmatrix} f_1 \\ f_2 \end{bmatrix},$$

where the diagonal blocks A_{ii} encode the self-interaction of the BIE operator on the i -th torus, the off-diagonal blocks A_{ij} ($i \neq j$) capture the coupling between the two tori, and f_i denotes the restriction of the incident field to the i -th torus. The module $\rho_{\theta(i)}$ represents $\rho_{i,N}$, and the off-diagonal blocks couple the two modules during training. Since a wider and deeper network provides a larger effective neural tangent space, each module contains 10 hidden layers of 500 neurons.

Table 4 records the training progression.

Scattering by a 3-torus. We solve the Helmholtz equation exterior to a genus-three surface, with the BIE discretized through the IBIM. The surface is defined by a dense point cloud. The incident field is the plane wave $u^{inc} = \exp(i\kappa y)$, with a chosen wave number κ .

Table 4: MLSG (progressive) training statistics for the linked-tori example. The epoch and time columns report the mean and standard deviation over 20 trials in separate sub-columns.

Level	Problem size	Target loss	# epochs		Time (s)	
			Mean	Std	Mean	Std
0	$1\,024 \times 2$	4×10^{-4}	556.30	23.39	3.64	0.53
1	$1\,600 \times 2$	4×10^{-4}	654.10	38.22	4.41	0.24
2	$2\,500 \times 2$	4×10^{-4}	492.30	37.86	4.31	0.34
3	$4\,096 \times 2$	2×10^{-4}	867.35	48.43	12.92	0.73
4	$6\,561 \times 2$	2×10^{-4}	851.75	66.63	25.94	2.03
5	$10\,404 \times 2$	2×10^{-4}	517.90	59.96	41.57	4.81
6	$16\,384 \times 2$	2×10^{-4}	348.30	38.76	58.79	6.56
7	$25\,921 \times 2$	2×10^{-4}	457.90	41.10	204.93	18.36
8	$41\,209 \times 2$	1×10^{-4}	1,216.05	47.29	1,321.14	51.43
9	$65\,536 \times 2$	1×10^{-4}	206.15	2.74	543.20	7.71
Total			6,168.10	271.61	2,220.87	62.73

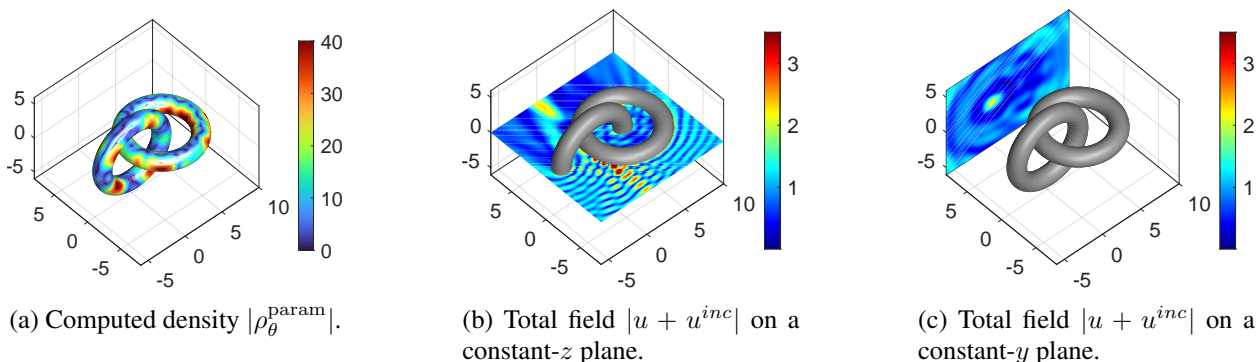

 Figure 8: Linked-tori Helmholtz problem ($\kappa = 4$) with a zero Neumann boundary condition and an incident plane wave in the x -direction.

Figure 9a shows the 3-genus computational domain, where the incident plane wave propagates in the x -direction. The domain is discretized with $n = 128$ grid points per dimension ($h \approx 0.2197$), and the Helmholtz equation is solved with wavenumber $\kappa = 3$. The neural network consists of 10 hidden layers with 500 neurons each, using a SIREN activation with $\omega_0 = 10$.

Table 5 reports the MLSG training statistics under the cyclic schedule.

Every stage of the cyclic schedule converged below its target loss. The schedule visits level 5 at a looser tolerance and revisits levels 4 and 5 with tightened tolerances (boldface rows in Table 5) before ascending to the finest grid. These revisits cost only a few seconds yet substantially reduce the work at the finest level, which then requires only 102.40 ± 4.17 epochs (29.69 s). The total wall-clock time is 47.72 ± 1.81 s with a small run-to-run spread, consistent with the variance reduction observed in Section 4.1.

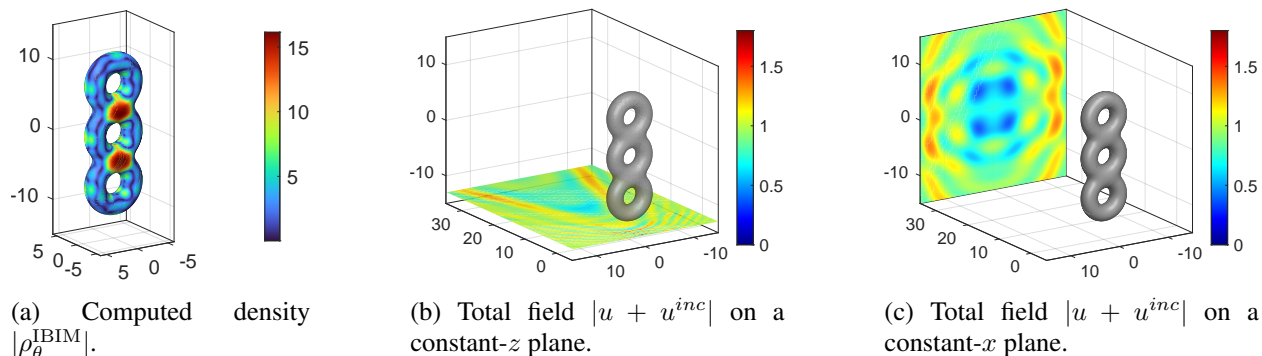


Figure 9: Three-genus Helmholtz problem ($\kappa = 3$) with a zero Neumann boundary condition and an incident plane wave in the x -direction.

Table 5: Training statistics under the cyclic schedule for the 3-genus Helmholtz problem ($n = 128$, $\kappa = 3$, 10 layers, 500 neurons/layer, Neumann BC). The epoch and time columns report the mean and standard deviation over 20 trials in separate sub-columns. The Total row reports the mean and standard deviation of the per-trial totals.

Level	Grid	Problem size	Target loss	# epochs		Time (s)	
				Mean	Std	Mean	Std
0	32^3	2 232	5×10^{-3}	73.05	8.47	0.48	0.24
1	40^3	3 512	5×10^{-3}	40.75	1.27	0.30	0.00
2	50^3	5 628	5×10^{-3}	36.15	0.79	0.40	0.00
3	64^3	9 264	3×10^{-3}	42.55	6.14	1.18	0.16
4	81^3	15 198	3×10^{-3}	27.85	0.81	1.41	0.07
5	102^3	24 034	3×10^{-3}	32.80	10.69	3.79	1.04
4	81^3	15 198	1×10^{-3}	49.00	3.29	2.52	0.17
5	102^3	24 034	1×10^{-3}	68.35	8.93	7.96	1.04
6	128^3	38 265	1×10^{-3}	102.40	4.17	29.69	1.20
Total				472.90	11.36	47.72	1.81

5 Concluding remarks

The multilevel stochastic-gradient neural solver (MLSG) solves second-kind boundary integral equations (1) by minimizing a discrete residual on a ladder of refining quadrature grids, with each stage warm-started from the previous one. Section 3.5 bounds the residual at the start of level $\ell + 1$ by the residual at the end of level ℓ plus a quadrature-change term, and gives a total work bound of $\mathcal{O}(bN_L)$ under Assumption 3.1, with N_L the finest grid and b the mini-batch size.

On the exterior Neumann Helmholtz problem, the MLSG attains substantial wall-clock speedups over multi-core GMRES (Table 3); GMRES slows as κ grows while the MLSG’s training cost stays nearly flat. Most of this gain comes from the multilevel schedule, not from the network alone: the leading band of $T_{\theta,N}$ resolved by training widens as the grid refines, and content outside $\mathcal{E}_\theta^{(\ell)}$ at level ℓ enters $\mathcal{E}_\theta^{(\ell+1)}$ at the next level and is damped there. The well-conditioning of the second-kind operator completes the picture:

$A_N^* A_N$ contributes only a bounded factor to the per-mode contraction rate (34), so the NTK is the sole rate-determining spectrum and its leading eigenvalues translate directly into fast residual decay.

The frequency principle of [16, 19] reports that, on a fixed grid, the high-frequency components of the residual contract last and often fail to contract at all within practical training budgets. The near-stationarity trap (S2) in Section 3.4 is its single-level expression. The MLSG clears it by refinement: at the warm start $\theta^{(\ell+1, \text{init})} = \theta^{(\ell, \text{end})}$, the sample on $\Gamma^{\ell+1}$ resolves more of the continuum NTK spectrum than the level- ℓ sample, so the refined-level gradient is generically nonzero. The slow NTK tail at any one resolution is not a hard accuracy limit for multiscale problems; a coarse-to-fine cascade reaches what no single grid can.

Acknowledgements

Bing-Ze Lu received support from the National Science and Technology Council, Taiwan, through Grants 113-2917-I-564-033 and 114-2115-M-194-007-MY3. Richard Tsai is supported partially by National Science Foundation grant DMS-2513857. Part of the research is also supported by the Swedish Research Council under grant no. 2021-06594, while Tsai was in residence at Institut Mittag-Leffler in Djursholm, Sweden during the Fall 2025 semester. This work used the Texas Advanced Computing Center (TACC) at The University of Texas at Austin for development and testing.

A Surface representations and discretization

This appendix collects the discretization details for the two surface representations of Section 4.

A.1 Parametric atlas

The atlas $\{(D_\alpha, \varphi_\alpha)\}_{\alpha=1}^{M_{\text{chart}}}$ of Section 4 satisfies

$$\Gamma = \bigcup_{\alpha=1}^{M_{\text{chart}}} \Gamma_\alpha, \quad \varphi_\alpha : D_\alpha \subset \mathbb{R}^{d-1} \longrightarrow \Gamma_\alpha \subset \Gamma, \quad (61)$$

with each φ_α a regular parametrization of the chart image Γ_α and the chart images pairwise disjoint up to a set of dS -measure zero (their common boundaries). The surface integral splits across charts as

$$\int_\Gamma f dS = \sum_{\alpha=1}^{M_{\text{chart}}} \int_{D_\alpha} f(\varphi_\alpha(\xi)) \mu_\alpha(\xi) d\xi, \quad \mu_\alpha(\xi) := \sqrt{\det(D\varphi_\alpha(\xi)^\top D\varphi_\alpha(\xi))}, \quad (62)$$

where μ_α is the chart-level surface element. The density on Γ is represented by one MLP per chart, written as the chart-indexed collection

$$\rho_\theta^{\text{param}} = (\rho_{\theta(1)}, \dots, \rho_{\theta(M_{\text{chart}})}), \quad \rho_{\theta(\alpha)} : D_\alpha \longrightarrow \mathbb{C}, \quad \theta(\alpha) \in \mathbb{R}^{p_\alpha}, \quad \alpha = 1, \dots, M_{\text{chart}}, \quad (63)$$

where $\theta(\alpha)$ collects the parameters of the chart- α network and the chart index is written in parentheses to keep it separate from the per-component subscript θ_k of Section 2.3. The full parameter vector $\theta = (\theta(1), \dots, \theta(M_{\text{chart}})) \in \mathbb{R}^p$ has dimension $p = \sum_{\alpha=1}^{M_{\text{chart}}} p_\alpha$. The surface density and the BIE data on chart α are

$$\rho(\varphi_\alpha(\xi)) = \rho_{\theta(\alpha)}(\xi), \quad g_\alpha(\xi) := g(\varphi_\alpha(\xi)), \quad \xi \in D_\alpha. \quad (64)$$

Atlas-level quadrature. Each chart carries its own quadrature on the parameter domain. On chart α we choose nodes $\{\xi_i^\alpha\}_{i=1}^{N_\alpha} \subset D_\alpha$ and positive weights $\{\omega_i^\alpha\}_{i=1}^{N_\alpha}$ such that

$$\int_{D_\alpha} \phi(\xi) \mu_\alpha(\xi) d\xi \approx \sum_{i=1}^{N_\alpha} w_i^\alpha \phi(\xi_i^\alpha), \quad w_i^\alpha := \omega_i^\alpha \mu_\alpha(\xi_i^\alpha),$$

which transports through φ_α to a quadrature on Γ_α with surface nodes $x_i^\alpha := \varphi_\alpha(\xi_i^\alpha)$ and weights w_i^α . The atlas-level node set, sample size, and weight matrix are

$$\Gamma_N = \bigsqcup_{\alpha=1}^{M_{\text{chart}}} \{x_i^\alpha\}_{i=1}^{N_\alpha}, \quad N = \sum_{\alpha=1}^{M_{\text{chart}}} N_\alpha, \quad W = \text{diag}(\{w_i^\alpha\}) \in \mathbb{R}^{N \times N}.$$

Substituting (64) into the second-kind BIE (1) and applying the resulting Q_N gives, for each $\alpha = 1, \dots, M_{\text{chart}}$ and $i = 1, \dots, N_\alpha$,

$$\frac{1}{2} \rho_{\theta(\alpha)}(\xi_i^\alpha) + \sum_{\beta=1}^{M_{\text{chart}}} \sum_{j=1}^{N_\beta} w_j^\beta k(\varphi_\alpha(\xi_i^\alpha), \varphi_\beta(\xi_j^\beta)) \rho_{\theta(\beta)}(\xi_j^\beta) = g_\alpha(\xi_i^\alpha), \quad (65)$$

the discrete equations on the atlas. For surfaces homeomorphic to circles (in 2D) or to tori (in 3D), the natural quadrature on each chart is a corrected truncated trapezoidal rule, chosen so as to handle the on-chart singularity of k consistently.

The two-chart system. We illustrate (65) for $M_{\text{chart}} = 2$. Collect the per-chart sample vectors and pulled-back data,

$$\rho_{N_\alpha}^{\text{param}} := (\rho_{\theta(\alpha)}(\xi_i^\alpha))_{i=1}^{N_\alpha} \in \mathbb{C}^{N_\alpha}, \quad g_{N_\alpha} := (g_\alpha(\xi_i^\alpha))_{i=1}^{N_\alpha} \in \mathbb{C}^{N_\alpha}, \quad \alpha = 1, 2,$$

and define the inter-chart kernel blocks

$$K^{\alpha\beta} \in \mathbb{C}^{N_\alpha \times N_\beta}, \quad (K^{\alpha\beta})_{ij} := w_j^\beta k(\varphi_\alpha(\xi_i^\alpha), \varphi_\beta(\xi_j^\beta)), \quad \alpha, \beta \in \{1, 2\}.$$

Then (65) is the block linear system

$$\underbrace{\begin{pmatrix} \frac{1}{2}I_{N_1} + K^{11} & K^{12} \\ K^{21} & \frac{1}{2}I_{N_2} + K^{22} \end{pmatrix}}_{=A_N} \begin{pmatrix} \rho_{N_1}^{\text{param}} \\ \rho_{N_2}^{\text{param}} \end{pmatrix} = \begin{pmatrix} g_{N_1} \\ g_{N_2} \end{pmatrix}, \quad (66)$$

with $W = \text{diag}(W_1, W_2)$, $W_\alpha := \text{diag}(w_1^\alpha, \dots, w_{N_\alpha}^\alpha)$, giving the weighted inner product on \mathbb{C}^N , $N = N_1 + N_2$. The diagonal blocks $K^{\alpha\alpha}$ contain the on-chart singular interactions and are evaluated with the singularity-aware quadrature; the off-diagonal blocks $K^{\alpha\beta}$, $\alpha \neq \beta$, are smooth in $(\xi_i^\alpha, \xi_j^\beta)$, so any standard product rule on $D_\alpha \times D_\beta$ suffices. The solver drives (66) through residual minimization on the concatenated parameters $\theta = (\theta(1), \theta(2))$, with $\rho_{\theta, N}$ in (16) replaced by the block vector $(\rho_{N_1}^{\text{param}}, \rho_{N_2}^{\text{param}})^\top$.

A.2 IBIM volumetric representation and tubular rule

When $\Gamma \subset \mathbb{R}^d$ is a closed C^2 surface given non-parametrically as the zero level set of a signed distance function d_Γ , we adopt the implicit boundary integral method (IBIM) of [15, 6]. The density on Γ is the trace of a single ambient MLP,

$$\rho_\theta^{\text{IBIM}} : \mathbb{R}^d \longrightarrow \mathbb{C}, \quad \rho(x) = \rho_\theta^{\text{IBIM}}(x), \quad x \in \Gamma, \quad (67)$$

optimized by the solver of Section 3.

The IBIM replaces the surface integral $\int_{\Gamma} f dS$ by a Cartesian-grid quadrature over a thin tubular neighborhood $T_{\epsilon} := \{x \in \mathbb{R}^d : |d_{\Gamma}(x)| < \epsilon\}$. The basic rule reads

$$\int_{\Gamma} f dS \approx \sum_{z_j \in T_{\epsilon}^h} h^d \delta_{\epsilon}(d_{\Gamma}(z_j)) J(z_j) f(P_{\Gamma}(z_j)), \quad (68)$$

where T_{ϵ}^h is the set of nodes of a Cartesian grid of spacing h inside T_{ϵ} , $P_{\Gamma}(z) := z - d_{\Gamma}(z) \nabla d_{\Gamma}(z)$ is the closest-point projection from T_{ϵ} onto Γ , $\delta_{\epsilon}(r) := \frac{1}{\epsilon} \eta(r/\epsilon)$ is a regularized delta formed from a fixed mollifier $\eta \in C_c^1([-1, 1])$ with $\int_{-1}^1 \eta = 1$ — for instance the raised cosine $\eta(s) = \frac{1}{2}(1 + \cos \pi s)$, giving $\delta_{\epsilon}(r) = \frac{1}{2\epsilon}(1 + \cos(\pi r/\epsilon))$ on $[-\epsilon, \epsilon]$ — and $J(z) := \prod_{i=1}^{d-1} (1 - d_{\Gamma}(z) \kappa_i(P_{\Gamma}(z)))$ is the Jacobian of the closest-point map relating the tubular volume element to the surface measure on Γ , with κ_i the principal curvatures of Γ [15]. With $\epsilon \gtrsim h$ the rule converges to $\int_{\Gamma} f dS$ as $h \rightarrow 0$, at an order set by the smoothness and moments of η . The atlas-level node set and weights are therefore

$$\Gamma_N = \{x_j = P_{\Gamma}(z_j) : z_j \in T_{\epsilon}^h\}, \quad w_j := h^d \delta_{\epsilon}(d_{\Gamma}(z_j)) J(z_j), \quad (69)$$

and the IBIM-discretized BIE operator $(\mathcal{K}\rho)(x) = \int_{\Gamma} k(x, y) \rho(y) dS(y)$ at quadrature nodes $x_i = P_{\Gamma}(z_i)$ is

$$(\mathcal{K}_N \rho)_i = \sum_{z_j \in T_{\epsilon}^h} w_j k(P_{\Gamma}(z_i), P_{\Gamma}(z_j)) \rho_{\theta}^{\text{IBIM}}(P_{\Gamma}(z_j)), \quad (70)$$

with near-diagonal entries (those for which $\|P_{\Gamma}(z_i) - P_{\Gamma}(z_j)\|$ is comparable to h) replaced by curvature-dependent constants following [15, 6]. High-order corrected trapezoidal IBIM rules are developed in [12]; the experiments of Section 4 use the basic rule (68).

We close by recording why the unweighted training loss of Section 4 is consistent for the IBIM discretization *independently of the mollifier* δ_{ϵ} . The point is that the unweighted loss is a Cartesian-grid quadrature of a tube-volume integral, which the tubular (co-area) change of variables ties to the surface L^2 norm.

Proposition A.1 (Unweighted IBIM loss as a tube-averaged surface norm). *Let $\Gamma \in C^2$ with $\epsilon \max_i \|\kappa_i\|_{\infty} < 1$, and let $\tilde{r} := r \circ P_{\Gamma}$ extend $r \in C(\Gamma)$ to T_{ϵ} . Then*

$$\int_{T_{\epsilon}} |\tilde{r}|^2 dx = \int_{\Gamma} |r(p)|^2 \omega_{\epsilon}(p) dS(p), \quad \omega_{\epsilon}(p) := \int_{-\epsilon}^{\epsilon} \prod_{i=1}^{d-1} (1 - s \kappa_i(p)) ds. \quad (71)$$

The fibre weight is independent of δ_{ϵ} and uniform to leading order; $\omega_{\epsilon}(p) = 2\epsilon(1 + \frac{\epsilon^2}{3} K_2(p) + O(\epsilon^4))$ with $K_2 := \sum_{i < j} \kappa_i \kappa_j$ (so $\omega_{\epsilon} \equiv 2\epsilon$ for $d = 2$, and $K_2 = K$ the Gaussian curvature for $d = 3$). Hence the unweighted loss $L(\theta) = \frac{1}{2} \sum_{z_j \in T_{\epsilon}^h} |\tilde{r}_{\theta}(z_j)|^2$, the Cartesian quadrature of $\frac{1}{2h^d} \int_{T_{\epsilon}} |\tilde{r}_{\theta}|^2$, approximates the surface loss $\frac{1}{2} \|r_{\theta}\|_{L^2(\Gamma)}^2$ up to the global factor $2\epsilon/h^d$ and a relative $\mathcal{O}(\epsilon^2)$ curvature distortion, with the same minimizer and without reference to the mollifier δ_{ϵ} (hence to its spread κ_W).

Proof. The normal map $x = p + s n(p)$ is a C^1 diffeomorphism $T_{\epsilon} \rightarrow \Gamma \times (-\epsilon, \epsilon)$ when $\epsilon \max_i \|\kappa_i\|_{\infty} < 1$, with $dx = \prod_{i=1}^{d-1} (1 - s \kappa_i(p)) ds dS(p)$. Since \tilde{r} is constant along each fibre, integrating in s gives (71), the odd-in- s terms vanishing over $[-\epsilon, \epsilon]$; the discrete statement is the midpoint quadrature of its left-hand side. \square

References

- [1] P. M. Anselone. *Collectively Compact Operator Approximation Theory and Applications to Integral Equations*. Prentice-Hall, Englewood Cliffs, NJ, 1971.
- [2] A. Atanasov, B. Bordelon, and C. Pehlevan. Neural networks as kernel learners: The silent alignment effect. In *International Conference on Learning Representations (ICLR)*, 2022.
- [3] K. E. Atkinson. *The Numerical Solution of Integral Equations of the Second Kind*. Cambridge University Press, Cambridge, 1997.
- [4] F. A. Bornemann and P. Deuffhard. The cascadic multigrid method for elliptic problems. *Numerische Mathematik*, 75(2):135–152, 1996.
- [5] A. J. Burton and G. F. Miller. The application of integral equation methods to the numerical solution of some exterior boundary-value problems. *Proceedings of the Royal Society of London. Series A*, 323(1553):201–210, 1971.
- [6] C. Chen and R. Tsai. Implicit boundary integral methods for the Helmholtz equation in exterior domains. *Research in the Mathematical Sciences*, 4(19), 2017.
- [7] H. Cheng, L. Greengard, and V. Rokhlin. A fast adaptive multipole algorithm in three dimensions. *Journal of Computational Physics*, 155(2):468–498, 1999.
- [8] D. Colton and R. Kress. *Integral Equation Methods in Scattering Theory*. SIAM, Philadelphia, 2013.
- [9] L. Greengard and V. Rokhlin. A fast algorithm for particle simulations. *Journal of Computational Physics*, 73(2):325–348, 1987.
- [10] W. Hackbusch. *Multi-Grid Methods and Applications*. Springer, Berlin, 1985.
- [11] W. Hackbusch. A sparse matrix arithmetic based on \mathcal{H} -matrices. Part I: Introduction to \mathcal{H} -matrices. *Computing*, 62(2):89–108, 1999.
- [12] F. Izzo, O. Runborg, and R. Tsai. Corrected trapezoidal rules for singular implicit boundary integrals. *Journal of Computational Physics*, 461:111193, 2022.
- [13] D. P. Kingma and J. Ba. Adam: A method for stochastic optimization. In *International Conference on Learning Representations (ICLR)*, 2015.
- [14] R. Kress. *Linear Integral Equations*. Springer, New York, 3rd edition, 2014.
- [15] C. Kublik, N. M. Tanushev, and R. Tsai. An implicit interface boundary integral method for Poisson’s equation on arbitrary domains. *Journal of Computational Physics*, 247:279–311, 2013.
- [16] N. Rahaman, A. Baratin, D. Arpit, F. Draxler, M. Lin, F. Hamprecht, Y. Bengio, and A. Courville. On the spectral bias of neural networks. In *Proceedings of the 36th International Conference on Machine Learning (ICML)*, pages 5301–5310, 2019.
- [17] Y. Saad and M. H. Schultz. GMRES: A generalized minimal residual algorithm for solving nonsymmetric linear systems. *SIAM Journal on Scientific and Statistical Computing*, 7(3):856–869, 1986.
- [18] V. Sitzmann, J. N. P. Martel, A. W. Bergman, D. B. Lindell, and G. Wetzstein. Implicit neural representations with periodic activation functions. In *Proceedings of the 34th International Conference on Neural Information Processing Systems, NIPS ’20*, Red Hook, NY, USA, 2020. Curran Associates Inc.

- [19] Z.-Q. J. Xu, Y. Zhang, T. Luo, Y. Xiao, and Z. Ma. Frequency principle: Fourier analysis sheds light on implicit regularization of deep neural networks. *Communications in Computational Physics*, 28(5):1746–1767, 2020.